# Fundamental physics measurements with Galileo FOC satellites and the Galileo for science project. II. A box wing for modeling direct solar radiation pressure and preliminaries orbit determinations

Feliciana Sapio,[1,2,3] David Lucchesi,[1,3,4,*] Massimo Visco,[1,3] Roberto Peron,[1,3] Marco Lucente,[1,3] Carlo Lefevre,[1] Marco Cinelli,[1] Alessandro Di Marco,[1] Emiliano Fiorenza,[1] Pasqualino Loffredo,[1] Carmelo Magnafico,[1,3] Francesco Santoli,[1] and Francesco Vespe[5]

[1]*Istituto Nazionale di Astrofisica (INAF), Istituto di Astrofisica e Planetologia Spaziali (IAPS), Via del Fosso del Cavaliere, 100, 00133 Roma, Italy*
[2]*Dipartimento di Fisica, Sapienza Università di Roma, Piazzale Aldo Moro 5, 00185 Roma, Italy*
[3]*Istituto Nazionale di Fisica Nucleare (INFN), Sezione di Tor Vergata, Via della Ricerca Scientifica 1, 00133 Roma, Italy*
[4]*Istituto di Scienza e Tecnologie della Informazione (ISTI), Consiglio Nazionale delle Ricerche (CNR), Via G. Moruzzi 1, 56124 Pisa, Italy*
[5]*Agenzia Spaziale Italiana (ASI), Centro di Geodesia Spaziale (CGS), Contrada Terlecchia, 75100 Matera, Italy*

(Received 16 July 2023; accepted 26 January 2024; published 12 March 2024)

This paper concerns the development of a first simplified model to take into account the perturbations produced by the nongravitational forces acting on the satellites of the Galileo FOC constellation and the corresponding first orbital determinations within the G4S_2.0 project. G4S_2.0 has a series of objectives in verifying the gravitational interaction in the weak field limit of the theory of general relativity, exploiting in particular the eccentricity of the orbits of some Galileo FOC satellites and the precise measurements that can be derived from the atomic clocks on board these satellites. The study focused on the model for the acceleration produced by direct solar radiation pressure on the satellites. This is the largest of all nongravitational perturbations. It is therefore necessary to build a sufficiently accurate model for it before being able to seriously consider smaller perturbation effects, such as those related to terrestrial radiation and thermal thrust effects. The work presents new aspects in the literature of navigation satellites. One of these is the determination of the effects in the Keplerian elements produced by the direct solar acceleration obtained from a box-wing model of the satellite. A second aspect is the comparison of these predictions in the orbital elements with the corresponding orbital residuals achieved from an orbit determination of the satellite. The study therefore highlights even more the importance of being able to improve the model of the perturbation originating from solar radiation in the field of global navigation satellite systems. This is very important if one wants to extract gravitational measurements from the orbit and clock-bias measurements of these satellites to verify the predictions of general relativity and compare them with those of alternative theories of gravitation.

DOI: 10.1103/PhysRevD.109.062005

## I. INTRODUCTION

This paper mainly focuses on modeling direct solar radiation pressure (SRP) on the current constellation of ESA Galileo FOC satellites and constitutes the continuation of a work presented in this same issue [1]. In particular, we introduce the results obtained for the effects of SRP in the case of a box-wing model of the spacecraft obtained according to the metadata of ESA Galileo FOC satellites [2]. Although not new in the literature of the global navigation satellite systems (GNSS), our box-wing (BW) model presents, in its various applications, several new aspects compared to what has already been published for the Galileo satellites, see for instance Bury *et al.* [3,4]. As explained in [1], this activity falls within the Galileo for Science (G4S_2.0) project funded by the Italian Space Agency (ASI) [5–8]. The main goals of G4S_2.0 are in the field of fundamental physics and exploit the relatively high eccentricity of the orbits of the Galileo GSAT0201 and GSAT0202 satellites and the accuracy of the on board atomic clocks, see [1] for details.

As said above, we are interested to model the effects of direct SRP on the Galileo FOC spacecraft. SRP represents the largest Non Gravitational Perturbation (NGP) on all GNSS satellites: about two orders of magnitude larger than the albedo perturbation, the second in magnitude. In fact,

*david.lucchesi@inaf.it

 

as we have extensively illustrated in [1] (see Secs. II and IV therein), suboptimal modeling of SRP is currently the main source of error in determining the orbits of all GNSS satellites. Therefore, being able to improve the model for the SRP of Galileo satellites is extremely important for a number of different reasons, such as: (i) the use of the orbits and clocks of these satellites for the products of the International GNSS Service (IGS) ([9]), (ii) for more purely geophysical and geodetic applications within the global geodetic observing system (GGOS) [10], (iii) and for applications in the field of fundamental physics of current and next generation satellites [5,11,12].

In [1] (hereafter Paper I), we described, in particular, how we built our 3D model of the current Galileo FOC spacecraft (see Sec. XII A) and our BW model based on ESA metadata (see Sec. XII). In particular, we introduced what we called a simplified box-wing (S-BW) model and we provided its first applications within COMSOL [13] (see Section XII B). As explained in Paper I, the 3D model will be used to calculate the impact of the SRP—as well as that of the Earth's radiation pressure—using a refined ray-tracing technique. This will only be possible once a much more in-depth characterization of the spacecraft is achieved than current knowledge based on presently available ESA metadata. This will be, in fact, our ultimate goal within G4S_2.0. In this work we will present the results of our analytical S-BW model in the case of direct solar radiation.

Another object of our investigations, which will be presented in the second part of this work, concerns the orbital determination of the Galileo FOC satellites. In fact, after the improvement of the dynamic model, precise orbit determination (POD) represents the main tool with which to obtain, directly or indirectly, the various gravitational measurements of interest for our project. These measurements can directly concern the knowledge of the state vector of the satellites, as in the case of those related to relativistic precessions, or a better estimate of the clock-bias of the on board atomic clocks, as in the case of local position invariance tests or to set constraints in the presence of dark matter.

The rest of the paper is organized as follows. Section II defines the main characteristics of the Galileo FOC satellites that we have taken into consideration for our analyses. In this section the attitude law applied to these satellites is also introduced and described. Section III defines the model we have adopted for the interaction of incoming solar radiation with the surfaces of the spacecraft. The accelerations produced by SRP on satellites in elliptical orbits are calculated using the S-BW model. In particular, the acceleration results are provided in different reference frames and under different representations. Section IV exploits the results obtained for the accelerations in the Gauss reference frame to determine their effects in the orbital elements of the aforementioned satellites. In Sec. V, on the basis of a very simplified dynamical model, we introduce our preliminary orbital determination for a Galileo satellite in elliptical orbit and for one in nominal orbit and we compare and discuss the obtained results. In particular, the orbital residuals of GSAT0201 have been computed and compared with the prediction of the S-BW model. In Sec. VI, we summarize the results obtained by interpreting them in terms of the further efforts to be made in the development of the dynamic model of the Galileo FOC satellites in order to achieve the fundamental physics objectives of G4S_2.0. Finally, in Sec. VII our conclusions and recommendations are provided.

## II. THE GALILEO FOC SATELLITES

In the present work we will apply our S-BW model to the two aforementioned satellites GSAT0201 and GSAT0202 in elliptical orbit. The application of the model to GSAT0206 and GSAT0208, which are instead in their nominal (almost circular) orbit, will be provided later. The reason why our analyzes and simulations focus on these two different types of Galileo FOC satellites lies precisely in the nature of the different fundamental physics objectives of the G4S_2.0 project.

As introduced in Paper I, elliptical orbits are particularly important for the modulation of the gravitational redshift signal and for the measurement of the total relativistic advancement of the satellite's argument of pericenter. From the latter it is possible to measure the Schwarzschild and Lense-Thirring precession and, consequently, to place constraints on alternative theories of gravitation through their predictions on the relativistic advancement of the pericenter of the orbits [14–19]. Conversely, the satellites in nominal orbit (together with the two satellites in elliptical orbit), in particular the atomic clocks on board these satellites, will be useful for placing constraints on the possible presence of dark matter in the spherical halo in which our galaxy is immersed and for the possibility of detecting in future gravitational waves by the use of all the satellites of the constellation [20].

In both cases, an improved POD of these satellites with respect to the current state of the art is mandatory to achieve precise and accurate measurements in the field of fundamental physics. Therefore, as already underlined, one of our objectives in this direction is to improve the dynamic model of the orbits of satellites and, first of all, that of the nonconservative forces starting from the SRP. In Table I, some physical characteristics of the satellites and of their orbits are shown together with their identification numbers.

In addition to the satellite name [21], the Table shows two different numbers to identify each satellite: the pseudorandom noise (PRN) number and the space vehicle number (SVN). The mean Keplerian elements $(a, e, i)$, those at the reference date $(\Omega_0, \omega_0, M_0)$ and their rate $(\dot{\Omega}, \dot{\omega}, \dot{M})$, are exactly those provided in the ESA metadata [22]. The slot indicates the orbital plane of each

TABLE I. Characteristics and orbital parameters of Galileo FOC satellites, mainly adapted from ESA Galileo metadata. The reference date for the satellites is November 21, 2016 at 00:00:00 UTC. Semi-major axis, eccentricity and inclination must be considered as mean values and not as obsculating elements. The metadata provides the indicated values for the mass of the satellites for December 2021 (see Sec. III for the mass values after the maneuvers of the satellites).

| Type | Eccentric orbit | Nominal orbit | Nominal orbit |
|---|---|---|---|
| Name | GSAT0201, GSAT0202 | GSAT0206 | GSAT0208 |
| PRN | E18, E14 | E30 | E08 |
| SVN | E201, E202 | E206 | E208 |
| Slot | Ext01, Ext02 | A05 | C07 |
| Launch dates | August 22, 2014 | September 11, 2015 | December 17, 2015 |
| Mass: $m$ (kg) | 660.977, 662.141 | 707.735 | 709.138 |
| Average cross-section: $A_\odot$ ($m^2$) | 13.210 | 13.210 | 13.210 |
| Semi-major axis: a (km) | 27977.6 | 29599.8 | 29599.8 |
| Eccentricity: e | 0.162 | 0.0 | 0.0 |
| Inclination: i (°) | 49.850 | 56.0 | 56.0 |
| RAAN: $\Omega_0$ (°) | 52.521 | 317.632 | 197.632 |
| Argument of pericenter: $\omega_0$ (°) | 56.198 | 0.0 | 0.0 |
| Mean anomaly: $M_0$ (°) | 316.069, 136.069 | 0.153 | 120.153 |
| $\dot{\Omega}$ (°/d) | −0.03986760 | −0.02764398 | −0.02764398 |
| $\dot{\omega}$ (°/d) | +0.03383184 | 0.0 | 0.0 |
| $\dot{M}$ (°/d) | +667.86467481 | +613.72253566 | +613.72253566 |
| Revolution period: P (h) | 12.94 | 14.08 | 14.08 |

satellite—A, B, C for satellites in nominal orbit and "Extended" for satellites in elliptical orbit—with the progressive number (up to a maximum of 8 for satellites in nominal orbit) of the satellites in that plane. The average cross section, $A_\odot$, is that seen from the Sun. It was estimated by adding the average cross section of the bus as seen from the Sun (2.390 $m^2$) to the surface of the solar panels (10.820 $m^2$).

### A. The Galileo FOC attitude law

The knowledge of the position of the spacecraft's center-of-mass (c.m.) [23] is not enough to describe the motion of a satellite of complex shape and equipped with antennas and motors, but it is also necessary to know the orientation of the spacecraft with respect to the inertial space. In Paper I, we briefly described the spacecraft attitude law. In the following, we will provide useful details on the basis of Galileo metadata and we will see the differences in the application of this attitude law between satellites in nominal orbit and those in elliptical orbit. In fact, in the case of GNSS satellites the knowledge of their attitude is very important for different reasons.

At first, because the navigation signals come from the phase center of the antenna (PCA), whose position does not coincide with that of the c.m. and, consequently, it is necessary to refer these microwave measurements to the c.m., i.e., the distance between the two points must be known. This distance in general is not constant due to fuel sloshing or mechanical movements of some Appendices, as in the case of solar panels. Anyway, even assuming the vector between these two points constant in magnitude, its orientation in inertial space changes due to the attitude law and its evolution needs to be known to correctly analyze navigation signals [24,25]. The same considerations on the microwave antennas and their PCA apply as well to the laser retroreflector array (LRA) used for satellite laser ranging (SLR). A third aspect is related to the so-called phase wind-up effect. This is related to the knowledge of the observed carrier phase, the latter depending on the relative orientation between the spacecraft and its antennas with the transmitted or received signals, which are right-handed circular polarized: this is the phase wind-up effect [26,27]. Finally, and this represents the aspect to which we are most interested in this work, the modeling of the direct SRP finds its implementation in the precise knowledge of the orientation of the spacecraft body and of the solar panels with respect to the incoming solar radiation [25,26].

For a GNSS spacecraft, the attitude is functional to the navigation task and to the corresponding requirements needed to guarantee it. In this regard, three drivers need to be satisfied [27]:

(1) The antenna boresight needs to be kept toward the Earth's center to provide the proper coverage and signal strength to the on-ground receivers.
(2) The solar panels need to maximise the received solar radiation, by aligning them perpendicularly to the Sun direction.
(3) One of the spacecraft faces parallel to the antenna boresight and to the solar panel rotation axis should point opposite to the Sun, in order to ease the thermal stability of atomic clocks (located close to this position).

The result of these requirements is the implementation of the yaw-steering (YS) mode, first implemented by GPS [28] and later by most other constellations. Such an approach is of course followed as well by the Galileo satellites [29].

It is assumed a body reference frame with $+Z$-axis aligned with the antenna boresight direction, $+Y$-axis parallel to the rotation axis of the solar panels and the $-X$-axis chosen so that the $-X$-panel is illuminated by the Sun during nominal YS, while the $+X$-panel is oriented toward deep space (the opposite for the other constellation). In order to follow the three drivers, the attitude requires a rotation of the spacecraft body about the Earth pointing $+Z$-axis (yaw axis) as well as a rotation of the solar panels about the $+Y$-axis (pitch axis) to be perpendicular to the Sun.

The typical attitude for GNSS spacecrafts is that of a nadir-pointing satellite, where the pitch and roll angles vanish and the spacecraft attitude is fully described by the yaw-angle $\Psi$; this is the reason of the name *yaw-steering* for the attitude mode. The yaw-angle $\Psi$ is function of just two angles: the Sun elevation $\beta_\odot$ with respect to the orbital plane and the position angle $\mu$ of the satellite on the orbital plane measured with respect to the midnight point or to the noon point:

$$\Psi = \mathrm{atan2}\left(\frac{-\tan\beta_\odot}{\sin\mu}\right), \tag{1}$$

where for the origin of $\mu$ we followed the first convention in agreement with [30], while atan2 refers to the range $(-\pi, +\pi)$ for the variability of the yaw-angle $\Psi$.

Following the ESA Galileo metadata, in the case of a Galileo FOC spacecraft, Eq. (1) takes the following expression:

$$\Psi = \mathrm{atan2}\left(\frac{\hat{s}(t)\cdot\hat{n}(t)}{\hat{s}(t)\cdot(\hat{r}(t)\times\hat{n}(t))}\right), \tag{2}$$

where

(i) $t$ is the current on-board computer time.
(ii) $\hat{s}(t)$ is the Sun position unit vector.
(iii) $\hat{r}(t)$ is the satellite position unit vector.
(iv) $\hat{n}(t)$ is the orbit normal unit vector.

and all these unit vectors are in the Earth centered inertial (ECI), J2000.0, reference frame.

However, the above law for the yaw-angle cannot be applied at all times during the life of a spacecraft due to technical limitations related to the performance of onboard reaction wheels. This happens during the eclipse season and, in particular, for small values of the $\beta_\odot$ angle (above or below the satellite's orbital plane) and near a collinear condition for the vectors that identify the Sun and the spacecraft with respect to the Earth, i.e., close to "midnight" ($\mu \simeq 0°$) and close to "noon" ($\mu \simeq 180°$). In these periods Galileo satellites (and GNSS in general) have to perform fast yaw-slews to accomplish the yaw angle change, i.e., an instantaneous rotation by 180° after crossing the orbit midnight or noon position.

Furthermore, being such an attitude law based on the use of solar sensors, the eclipse of the Sun in these periods may result in non-nominal yaw angles during limited periods of time. The result is that: (i) maneuvers at noon and midnight positions depart from the nominal attitude, causing a time delay between the current and the nominal yaw angle, and (ii) additional manoeuvres are needed to recover the nominal attitudes after the position crossings. Moreover, a further drawback during these phases is that the need to move the spacecraft with a high yaw-rate, or close to it, can excite solar array oscillations and/or propellant sloshing motion, inducing at the same time c.m. displacements. This produces a worst knowledge of the attitude, already degraded for the transitions and, finally, in several related aspects, as precise point positioning [31], tropospheric and clock solutions [26] and in the overall POD [32]. We refer to [27] for further details.

Consequently, in the case of the Galileo FOC satellites, when the satellite and Sun position vectors are close to collinearity, the following "modified" yaw steering law is used:

$$\Psi_{\mathrm{mod}}(t_{\mathrm{mod}}) = 90°\cdot\mathrm{sign} + (\Psi_{\mathrm{init}} - 90°\cdot\mathrm{sign})\cdot\cos\left(\frac{2\pi}{T_0}t_{\mathrm{mod}}\right), \tag{3}$$

where

(i) $t_{\mathrm{mod}}$ is the elapsed time since the switch over.
(ii) $\Psi_{\mathrm{init}}$ is the yaw-angle $\Psi(t)$ at the time of the switch over to the modified yaw profile.
(iii) sign is the sign of $\Psi_{\mathrm{init}}$.

Therefore, close to orbit noon and midnight, Eq. (3), allows to keep the yaw changing rate law compared to that provided by Eq. (1). The period $T_0 = 5656$ s corresponds to about two times the maximum duration of the noon/midnight maneuver.

As specified in the Galileo FOC metadata of ESA, the switch over to the modified yaw steering law takes place when all of the following conditions are met:

(i) The Sun elevation angle $\beta_\odot$ is smaller than the value $\beta_0 = 4.1°$.
(ii) The current collinearity angle $\epsilon$ is smaller than the value $\epsilon_0 = 10.0°$.
(iii) The collinearity angle for the previous epoch was bigger than $\epsilon_0$.

The collinearity angle $\epsilon$ is defined as follows:

$$\begin{cases} \epsilon = \arccos(\hat{r}\cdot\hat{y}) & \text{if } \arccos(\hat{r}\cdot\hat{y}) \le 90° \\ \epsilon = 180° - \arccos(\hat{r}\cdot\hat{y}) & \text{if } \arccos(\hat{r}\cdot\hat{y}) > 90°, \end{cases} \tag{4}$$

where

$$\begin{cases} \hat{x} = \hat{n} \times \hat{s} \\ \hat{y} = \hat{n} \times \hat{x} \end{cases} \tag{5}$$

In the following figures are shown the results for the attitude law in the case of GSAT0208 on the basis of the information provided in Table I and for a simulation period of 1 year. In Fig. 1 it is shown the comparison of the nominal and the modified yaw-steering law following ESA metadata, i.e., Eqs. (2) and (3). The two laws perfectly overlap outside the eclipse season, but show differences near and during eclipses. Also shown is the change in the height of the Sun, $\beta_\odot$, with respect to the orbital plane during the simulated period.

The differences between the two attitude laws are evident in Fig. 2, where the smoothest variation of the modified law with respect to the nominal law is clear and evident.

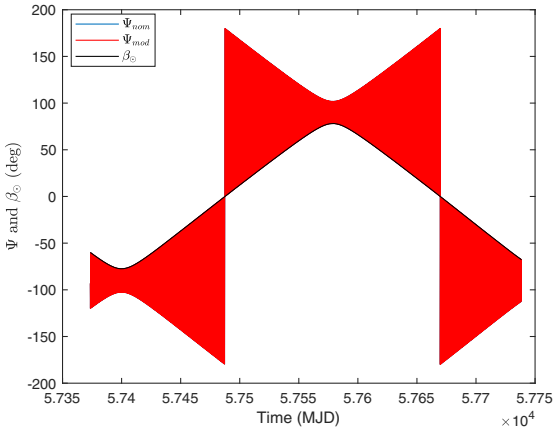


FIG. 1. Nominal (blue) and modified (red) attitude law for GSAT0208. Two eclipse seasons are shown. The starting epoch corresponds to November 21, 2016. The black line defines the variation of the Sun's altitude with respect to the orbital plane in the period shown.

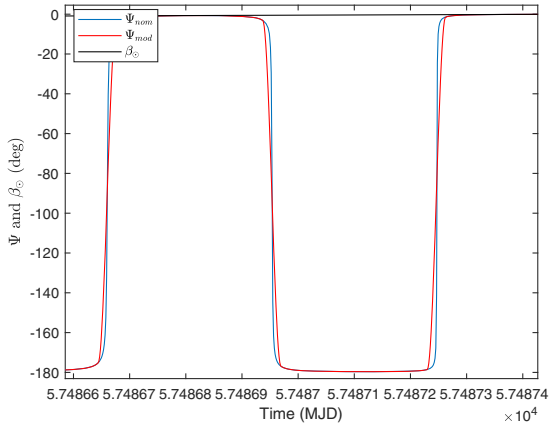


FIG. 2. Detail of the Fig. 1 close to the first eclipse season.

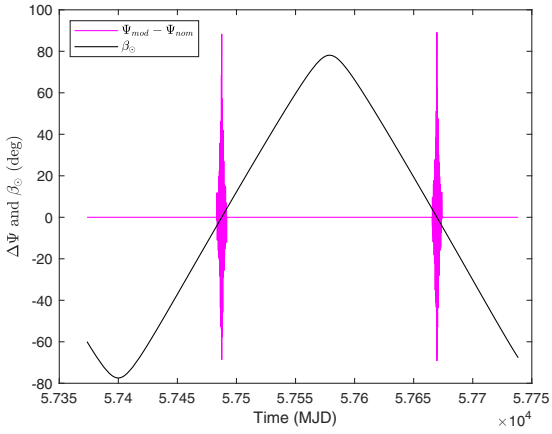


FIG. 3. Difference between the modified and nominal attitude laws for GSAT0208 together with the $\beta_\odot$ angle variation.

Figure 3 shows the difference between the modified law $\Psi_{\mathrm{mod}}$ and the nominal law $\Psi_{\mathrm{nom}}$. Clearly the differences are only along the eclipse seasons with the consequent nonorthogonality of the solar panels to the incoming solar radiation pressure.

It is important to underline that the attitude law described was designed for satellites in circular orbit, such as GNSS satellites in general, and not for satellites in elliptical orbit, such as GSAT0201 and GSAT0202. Currently, this attitude law is instead applied also to these satellites ([33]), and it is therefore not optimal for a profitable use of the tracking observations and for the PODs of these satellites during the eclipse season. In Figs. 4 and 5 the different behavior during the eclipses between GSAT0201, in elliptic orbit, and GSAT0208, in nominal (quasi circular) orbit, are shown.

The first figure provides the cosine of the angle between the solar panels normal and the direction of the incoming SRP. As can be derived, in the case of GSAT0208, the maximum fractional discrepancy from the orthogonality

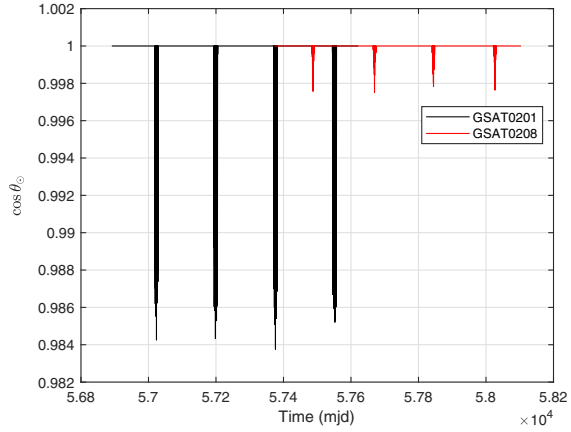


FIG. 4. Cosine of the angle between the normal to the solar panels and the direction of the incident solar radiation: comparison between GSAT0201 and GSAT0208.

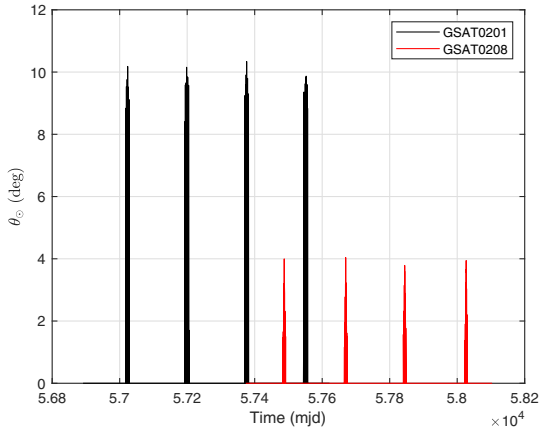


FIG. 5. Angle between the normal to the solar panels and the direction of the incident solar radiation: comparison between GSAT0201 and GSAT0208.

condition to the solar panels for incoming solar radiation is approximately 0.25%, increasing to 1.62% for GSAT0208. The second figure shows that this maximum discrepancy corresponds to an angle of about 10° for GSAT0201 and to about 4° in case of GSAT0208.

Therefore, in order to make the most of the data useful to the earth-segment from the satellites in elliptical orbit during the eclipses, one should proceed with a variation of the conditions linked to the modified attitude law described by Eq. (3), in particular acting on the collinearity angle $\epsilon_0$.

## III. SPACECRAFT-SOLAR RADIATION INTERACTION

In this section we apply the box-wing we have developed to the modeling of the direct SRP. This model is fully described in Section III B 4 of Paper I. We recall that it is a box-wing model that we have defined "simplified" (S-BW), since it is based on the current Galileo metadata [34], which provide a very rough approximation of the real satellite. The overall complex shape of the satellite bus—because of the instrumentation of the face pointing to the Earth plus the radiators on the other faces—and of the solar panels are approximated by a parallelepiped plus symmetric wings, and with average optical properties for five different materials, already introduced in Table VI of Paper I. Equation (6) provides the acceleration produced by the direct SRP on a elementary surface $dA$ of the spacecraft [35]:

$$\mathbf{da} = -\frac{\Phi_\odot}{mc}\left[(1-\rho)\hat{\mathbf{e}}_\mathbf{D} + 2\left(\frac{\delta}{3} + \rho\cos\vartheta\right)\hat{\mathbf{n}}\right] dA|\cos\vartheta|, \tag{6}$$

where $\Phi_\odot$ represents the solar irradiance, $m$ the mass of the satellite, $c$ the speed of light, the unit vector $\hat{\mathbf{e}}_\mathbf{D}$ is directed toward the Sun from the spacecraft center of mass, and finally $\hat{\mathbf{n}}$ represents the unit vector normal to the surface and $\vartheta$ the Sun zenith angle with respect to the surface normal, such that $\cos\vartheta = \hat{\mathbf{e}}_\mathbf{D}\cdot\hat{\mathbf{n}}$. The optical coefficients $\alpha$ (absorption), $\rho$ (specular reflection), and $\delta$ (diffusive reflection) satisfies the condition:

$$\alpha + \rho + \delta = 1, \tag{7}$$

which shows that each surface $dA$ behaves like a linear combination of an ideal black body, a perfect mirror, and a perfect diffuser. As explained in Paper I, we avoid the approximation that assumes instantaneous thermal reradiation for the absorbed radiation, as suggested by [36] and usually assumed in the GNSS literature [3,4,37]. We will address this aspect in a work dedicated to thermal effects. In fact, as highlighted in Paper I, these are characterized by a plethora of effects of different origins and act on the satellite with accelerations of the order of $10^{-10}\mathrm{m/s^2}$ or less. They can therefore be taken into serious consideration only after adequately modeling not only direct solar radiation, but also terrestrial albedo and infrared radiation pressure, see Table II.

In the following subsections we will present the results obtained for the accelerations produced by the SRP on the Galileo FOC satellite GSAT0201 characterized by an elliptical orbit. The results obtained in the case of GSAT0202 are provided in the Supplemental Material [39]. We will compare our results with those reported in the literature and, in particular, with those of Bury *et al.* [3,4], whenever possible. The simulations for the different satellites were carried out over a two-year period starting from the time of their launch, see Table I. An integration step of 120 s has been used. The eclipses have been modeled with a conical shadow model for a spherical Earth, in such a way to consider penumbra effects [40]. In our simulations we also considered the variation of the mass of the satellites, when occurs, as reported by the international laser ranging service (ILRS) [41], see Table III.

Table IV provides the Keplerian orbital elements of the satellites that we computed from the precise orbits of ESA determined at ESOC. This provides orbits more accurate than those reported in the ESA Galileo Metadata, which seem approximate or physically implausible for several orbital elements and their rates. Therefore, the satellites state-vector (position and velocity) calculated in the terrestrial rotating reference frame (sp3c files: Extended Standard Product-3 format) have been transformed, on the basis of current IERS Conventions [42]—i.e., taking into account for polar motion, precession and nutation—from the rotating frame to the J2000.0 inertial one. This state-vector was finally transformed into the corresponding six Keplerian elements. Finally, from the temporal evolution of the elements we estimated their corresponding rate. We have kept from the Galileo metadata only the information relating to the mean anomaly $M$ of the two satellites.

TABLE II. Main nongravitational accelerations (S.I. units) on a Galileo FOC satellite. The symbol $(\cdots)$ means that the acceleration is negligible, while the symbol (NA) means that the acceleration is currently unknown (not available), since it has not yet been evaluated. We refer to Paper I for more details.

| Physical effect | Formula | Parameter [S.I. units/adim] | Galileo FOC |
|---|---|---|---|
| Direct SRP | $C_R \frac{A}{m}\frac{\Phi_\odot}{c}$ | $\Phi_\odot = 1360.8$ | $1.0 \times 10^{-7}$ |
| Earth's Albedo | $2\frac{A}{m}\frac{\Phi_\odot}{c}A_\oplus \frac{\pi R_\oplus^2}{4\pi r^2}$ | $A_\oplus \approx 0.3$ | $7.0 \times 10^{-10}$ |
| Earth's infrared radiation | $\frac{A}{m}\frac{\Phi_{\rm IR}}{c}\frac{R_\oplus^2}{r^2}$ | $\Phi_{\rm IR} \approx 240$ | $1.1 \times 10^{-9}$ |
| Neutral drag | $\frac{1}{2}C_D\frac{A}{m}\rho V^2$ | $C_D, \rho$ | $\cdots$ |
| Charged drag | [38], Chap. 5 | Species densities, floating potential | ¬ |
| Power from antennas | $\frac{P}{mc}$ | $P \simeq 265$ | $1.2 \times 10^{-9}$ |
| Thermal effect solar panels | $\frac{2}{3}\frac{\sigma}{c}\frac{A}{m}(\epsilon_1 T_1^4 - \epsilon_2 T_2^4)$ | $\epsilon_1 \simeq \epsilon_2 \approx 0.8, T_1 \simeq 317, T_2 \simeq 318$ | $1.9 \times 10^{-10}$ |
| Y-bias | $Y_0$: empirical acceleration | $Y_0$ | $7.0 \times 10^{-10}$ |
| Poynting-Robertson | $\frac{1}{4}\frac{A}{m}\frac{\Phi_\odot}{c}\frac{R_\oplus^2}{r^2}\frac{v}{c}$ | $\Phi_\odot = 1360.8$ | $1.9 \times 10^{-14}$ |
| Solar Yarkovsky-Schach | $\frac{16}{9}\frac{A}{m}\frac{\epsilon\sigma}{c}T_0^3\Delta T$ | $\epsilon, T_0, \Delta T$ | ¬ |
| Earth Yarkovsky | $0.41\frac{4}{9}\frac{A}{m}\frac{\epsilon\Phi_{\rm IR} f_0}{\alpha c}\frac{R_\oplus^2}{r^2}$ | $\Phi_{\rm IR}, f_0, \alpha$ | ¬ |

TABLE III. Mass values for Galileo satellites FOC GSAT0201 (E18) and GSAT0202 (E14). These values for satellite masses are current as of December 20, 2022.

| Satellite | Time interval | Mass [kg] | Time interval | Mass [kg] |
|---|---|---|---|---|
| GSAT0201 | August 22, 2014 | 660.977 | | |
| GSAT0202 | August 22, 2014 to July 30, 2015 | 662.646 | July 31, 2015 to onward | 662.141 |

### A. Long-term analysis of the SRP accelerations: GSAT0201

Figure 6, shows the variation of the Sun's height $\beta_\odot$, over the 2-year period of the current simulation, with respect to the orbital plane of GSAT0201 together with the modified and nominal attitude law for $\Psi$, as described in the Galileo metadata.

It is precisely the evolution over time of the satellite attitude law, characterized by a long-term evolution mainly linked to the satellite's draconic year, and by higher-frequency evolutions, mainly at the orbital period of the satellite, which shapes the evolution over time of the perturbation linked to solar radiation.

The following figures show the impact of the accelerations due to the direct SRP in the case of the GSAT0201 satellite approximated with the S-BW model. The results are provided in three different frames of the satellite, see Fig. 7.

Figure 8 shows the acceleration in the DYB frame of the spacecraft, which is also known as the Sun-satellite-Earth (SSE) reference frame. The D-axis is defined by the unit vector $\hat{\mathbf{e}}_\mathbf{D}$ already introduced, $\hat{\mathbf{e}}_\mathbf{Y}$ is the unit vector along the spacecraft solar panel axis and defines the Y-axis, finally $\hat{\mathbf{e}}_\mathbf{B} = \hat{\mathbf{e}}_\mathbf{D} \times \hat{\mathbf{e}}_\mathbf{Y}$ defines a right-handed reference system and the corresponding B-axis. The overwhelming contribution of the acceleration along the D-axis is due to the interaction of direct SRP with the solar panels which, according to the attitude law described in Sec. II A, are always orthogonal to the solar rays except in periods characterized by eclipses. To a lesser extent, the interaction of solar radiation with the faces of the bus of the spacecraft contributes once the different contributions are projected along the D-axis.

As we can see from this figure, the maximum accelerations (in absolute value) along the D-axis are about two orders of magnitude greater than the accelerations along the B-axis. Indeed, the behavior of the acceleration along the

TABLE IV. Orbital elements for the Galileo FOC satellites GSAT0201 (E18) and GSAT0202 (E14) estimated from the Precise Orbits of ESOC. The reference date for the satellites is November 21, 2016 at 00:00:00 UTC.

| Satellite | $a$ [m] | $e$ | $I$ [°] | $\Omega$ [°] | $\omega$ [°] | $M$ [°] |
|---|---|---|---|---|---|---|
| GSAT0201 | 27978099.66 | 0.1604 | 50.369 | 53.505<br>−0.04000414086 [°/d] | 50.184<br>+0.04910776939 [°/d] | 316.069<br>+667.909221051 [°/d] |
| GSAT0202 | 27977624.83 | 0.1608 | 50.309 | 52.459<br>−0.04002923721 [°/d] | 52.086<br>+0.04784293004 [°/d] | 136.069<br>+667.909221051 [°/d] |

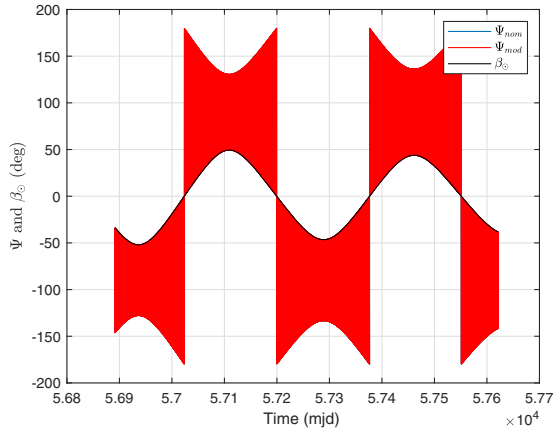


FIG. 6. GSAT0201 (E18): nominal (blue) and modified (red) attitude law. Four eclipse seasons are shown. The starting epoch corresponds to August 23, 2014. The black line defines the variation of the Sun's altitude with respect to the orbital plane in the period shown.

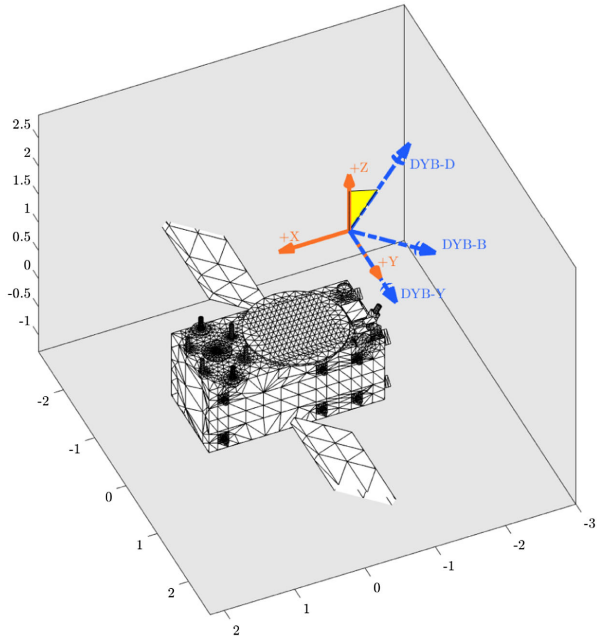


FIG. 7. Representations of the DYB and XYZ reference frames of the spacecraft. The yellow sector highlights the direction of the Sun along the +D axis compared to the +Z direction which instead points toward the Earth.

D-axis is very close to the behavior of the absolute value of the direct SRP on the S-BW model, see Fig. 9. Concerning the behavior of the acceleration along the Y-axis, this is the same as the one shown in Fig. 13: it is nonzero only during the eclipse season in this approximation for the orientation of the solar panels with respect to the incoming solar radiation pressure.

Figure 10, shows the behavior of the direct SRP acceleration in the Gauss comoving frame $(\hat{\mathbf{r}}, \hat{\mathbf{t}}, \hat{\mathbf{w}})$. In this

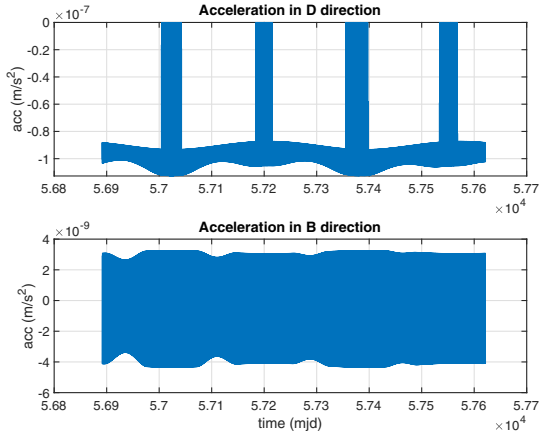


FIG. 8. GSAT0201 (E18): acceleration due to direct SRP along the D (top) and B (bottom) directions.

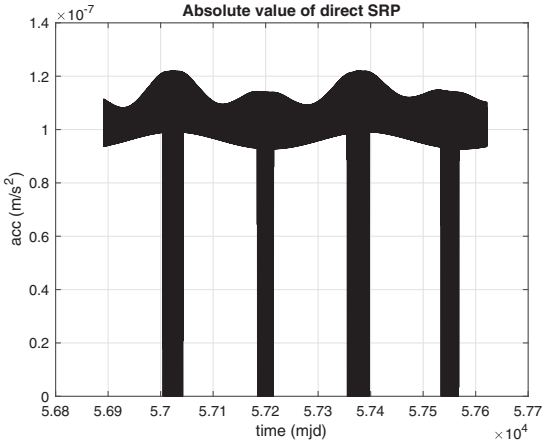


FIG. 9. GSAT0201 (E18): absolute value of the acceleration due to direct SRP.

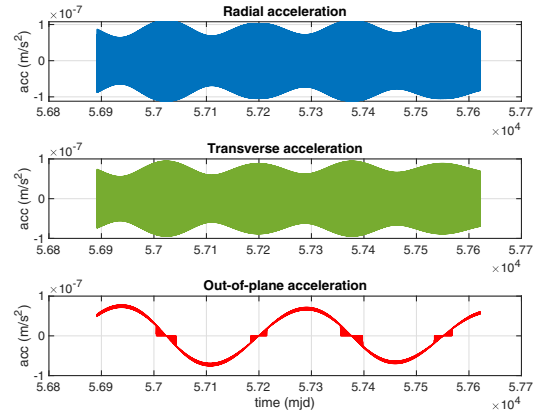


FIG. 10. GSAT0201 (E18): acceleration due to direct SRP along the directions of the Gauss comoving frame.

frame corotating with the satellite revolution around the Earth, the radial direction ($\hat{\mathbf{r}}$) is identified by the direction from the Earth's center of mass to the satellite center of mass. The out-of-plane or cross-track direction ($\hat{\mathbf{w}}$) is identified by the obsculating angular momentum direction. Finally, the transverse direction ($\hat{\mathbf{t}}$) is defined in such a way to define a right-handed reference system: $\hat{\mathbf{t}} = \hat{\mathbf{w}} \times \hat{\mathbf{r}}$. For our purposes, the introduction of the Gauss reference frame is important to express the perturbing effects of the modeled SRP in the so-called Gauss perturbing equations. This will allow us to estimate the impact of the disturbance effects on the orbital elements, see Sec. IV.

As we can see from Fig. 10, the radial $R$ and transverse $T$ accelerations have a similar behavior and magnitude. The maximum values for the out-of-plane $W$ acceleration are a little smaller and its long-term behavior is clearly modulated by the variation of the solar height with respect to the orbital plane. This long-term modulation is also present for the other two components, but for these components the modulation of the acceleration at the orbital period assumes a clear and evident importance. In Figs. 11 and 12 we compare these three components of the direct SRP in two very different conditions for the Sun height $\beta_\odot$: during a few eclipses (where the solar height is very close to zero) and far way from the eclipses (where the solar height is very close to its maximum value). Obviously, in the first case the out-of-plane component of the SRP acceleration is practically zero and its effects on the orbital elements are fully negligible. Conversely, in the second case the out-of-plane component is almost constant and greater than the other two components. Finally, the radial and transverse components have similar behavior in the two cases, as already anticipated.

Finally, Fig. 13 shows the components of direct SRP acceleration in the spacecraft frame already introduced in Sec. II A, the XYB frame. The $Y_B$-axis coincides with the solar panel axis Y-axis of the DYB frame and the $Z_B$-axis

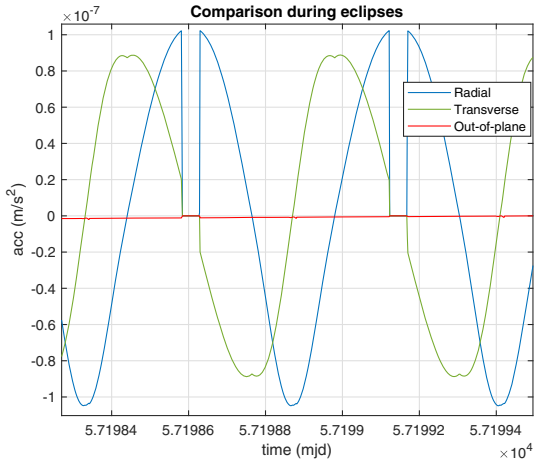


FIG. 11. GSAT0201 (E18): components of the Gauss perturbing acceleration due to direct SRP during eclipses.

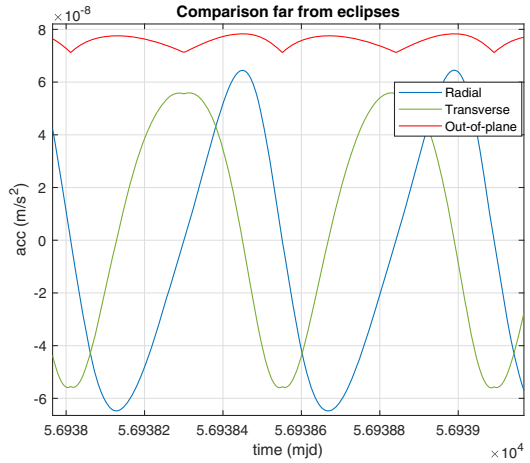


FIG. 12. GSAT0201 (E18): components of the Gauss perturbing acceleration due to direct SRP far from eclipses.

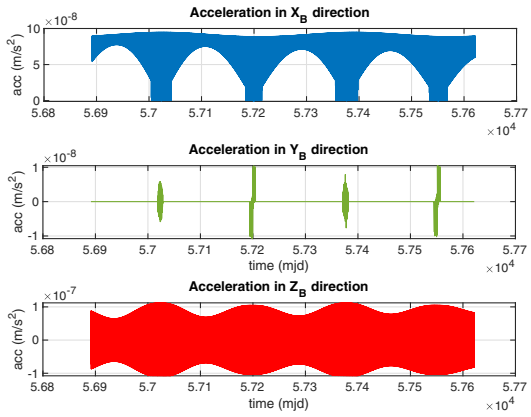


FIG. 13. GSAT0201 (E18): acceleration due to direct SRP along the spacecraft body axes.

is nadir pointing and opposite to the radial direction axis of the Gauss frame. The $X_B$-axis completes the right handed frame: $\hat{\mathbf{X}}_\mathbf{B} = \hat{\mathbf{Y}}_\mathbf{B} \times \hat{\mathbf{Z}}_\mathbf{B}$. In practice, the XYZ frame coincides with the mechanical reference frame introduced in Paper I.

This reference frame is interesting to consider in view of the possible on-board installation of an accelerometer in a next generation of Galileo satellites. This is one more goal of the G4S_2.0 project. In fact, the XYZ frame represents the reference integral with the satellite on which to orient the three axes of the accelerometer. An accelerometer of the right sensitivity and measurement band would in fact provide a direct measurement of the various nongravitational and inertial accelerations to which the satellite is subjected. Therefore, an on-board accelerometer will contribute improving the satellites POD, also using its measurements in synergy with the new models for NGPs.

In the next subsections we will deepen the description of the results obtained according to two different representations for the accelerations produced by direct solar radiation.

### *1. Synoptic view of the accelerations*

After introducing a representation in the time domain of the components of the acceleration produced by the SRP according to three different reference systems, in this section we are interested to introduce and discuss the representation of the components of the SRP according to two other different approaches. The first is a synoptic representation of the acceleration in the plane $(\Delta u, \beta_\odot)$, where $\Delta u = u - u_\odot$ is the difference between the argument of latitude $u$ of the satellite with respect to that of the Sun $u_\odot$. From the practical point of view, $\Delta u$ represents the azimuth of the satellite direction in the orbital plane with respect to the projection of the Sun direction in that plane. The second approach is instead based on the spectral analysis of the different components of the acceleration produced by the SRP, see Sec. III A 2. Both approaches are important to characterize accelerations more fully, as we will see, and to allow us to improve their modeling and, consequently, the final orbital determination of the satellite.

In Figs. 14(a) and 14(b) the synoptic representation of the accelerations produced by the direct SRP along the D and B directions are shown. We have restricted the representation to the first 200 days of our simulation, so as to contain a single excursion in the height of the Sun between its minimum and its maximum (whose periodicity is approximately 183 days). This allows us not to report on the plane the further acceleration variations linked to the variation—between the successive maximum and minimum values, of the height of the Sun due to the precession of the orbital plane—accelerations which would tend to stratify on the previous values "dirtying" the representation itself. The color bar provides the accelerations values in $m/s^2$.

In the case of the Figs. 14(a) and 14(b), the trend of the values traced for the accelerations depends on the variable geometry of the SSE reference frame, which is influenced by the variation of the solar height with respect to the orbital plane and its distance from the satellite, as well as by the different attitude of the spacecraft with respect to the Earth and the Sun.

This type of representation for accelerations is more useful than the one previously reported in the time domain when one wants to highlight the variations of the dynamic perturbation model with respect to a basic model taken as a reference. As we highlighted in Paper I, our ultimate goal is to develop a FEM for the Galileo-FOC and apply an *ad hoc* raytracing technique to calculate the different perturbative accelerations, starting from the direct SRP.

As a possible example of this aspect, we can compare our results in the D and B directions with the corresponding results obtained in [4]. We recall that these authors modeled the absorbed radiation assuming that it is instantaneously reemitted back to space according to Lambert's law, see Eq. (7) of Paper I. The authors assumed that this will make a difference for the bus but not for the solar panels, since they assumed the same temperature for the front and back sides of the panels. For geometric reasons, we expect this further acceleration to have a greater impact along the D direction and a lesser impact along the B direction, although not zero. Indeed, if we compare our Figs. 14(a) and 14(b) with Fig. 2 of [4], respectively (bottom left) and (bottom right), for the Galileo-FOC E18 satellite, we note that the most evident discrepancies occur along the D direction. Conversely, if we include in our model, i.e., in Eq. (6), the immediate thermal re-radiation to space of the absorbed radiation, we obtain the two representations of Figs. 14(c) and 14(d) for the accelerations along the D and B directions. In this case our Fig. 14(d) is practically indistinguishible from that of [4], while Fig. 14(c) still shows some differences related to the different attitude law modeled for the satellite: in [4] a perfect orthogonality between the solar panels with the direction of the incoming solar radiation has been assumed, this is reflected in evident differences when $\beta_\odot$ is close to zero.

In Figs. 14(e) and 14(f) we show the differences in the synoptic representation due to the contribution of the immediate thermal re-radiation of the absorbed radiation. Naturally, as already highlighted in the above discussion, the major differences occur in the case of direction D, see the acceleration values on the scale of the color bar.

### *2. Spectral analysis of the accelerations*

Figure 15 shows the different behavior for the two components of the acceleration along the D and B directions in the frequency domain. The fast Fourier transform (FFT) has been computed on the 2-year period of the analysis, but long-term effects (low frequencies) were not represented in the figure. The acceleration amplitude in the two components is expressed in terms of the frequency in Hz in a semilogaritmic scale. The spectral lines are at the orbital revolution frequency $f_{\mathrm{orb}} \simeq 2.15 \times 10^{-5}$ Hz and its integer multiples, and greater along the D direction, in accordance with the values reported in Figs. 8, 14(a), and 14(b). Indeed, as was reasonable to expect, the spectrum is characterized by larger amplitudes along the D direction—see for example the lines at 2, 3 and 4 times the orbital frequency—due to the attitude law and to the nadir pointing of the satellite, which make the contribution of the satellite bus more relevant. In these cases, the amplitudes of the acceleration are comparable at different frequencies: between $2 \times 10^{-9}$ $m/s^2$ and $4 \times 10^{-9}$ $m/s^2$. Conversely, in the case of acceleration along the B direction, the amplitudes of acceleration at higher frequency are much smaller than that at orbital frequency.

Figure 16 shows the different behavior for the two components of the acceleration along the X and Z directions in the frequency domain. The X-component of the SRP acceleration is dominated by a line at twice of the orbital frequency with an amplitude of about $1.95 \times 10^{-8}$ $m/s^2$, while the Z-component (or radial component) is dominated by a line at the orbital frequency with

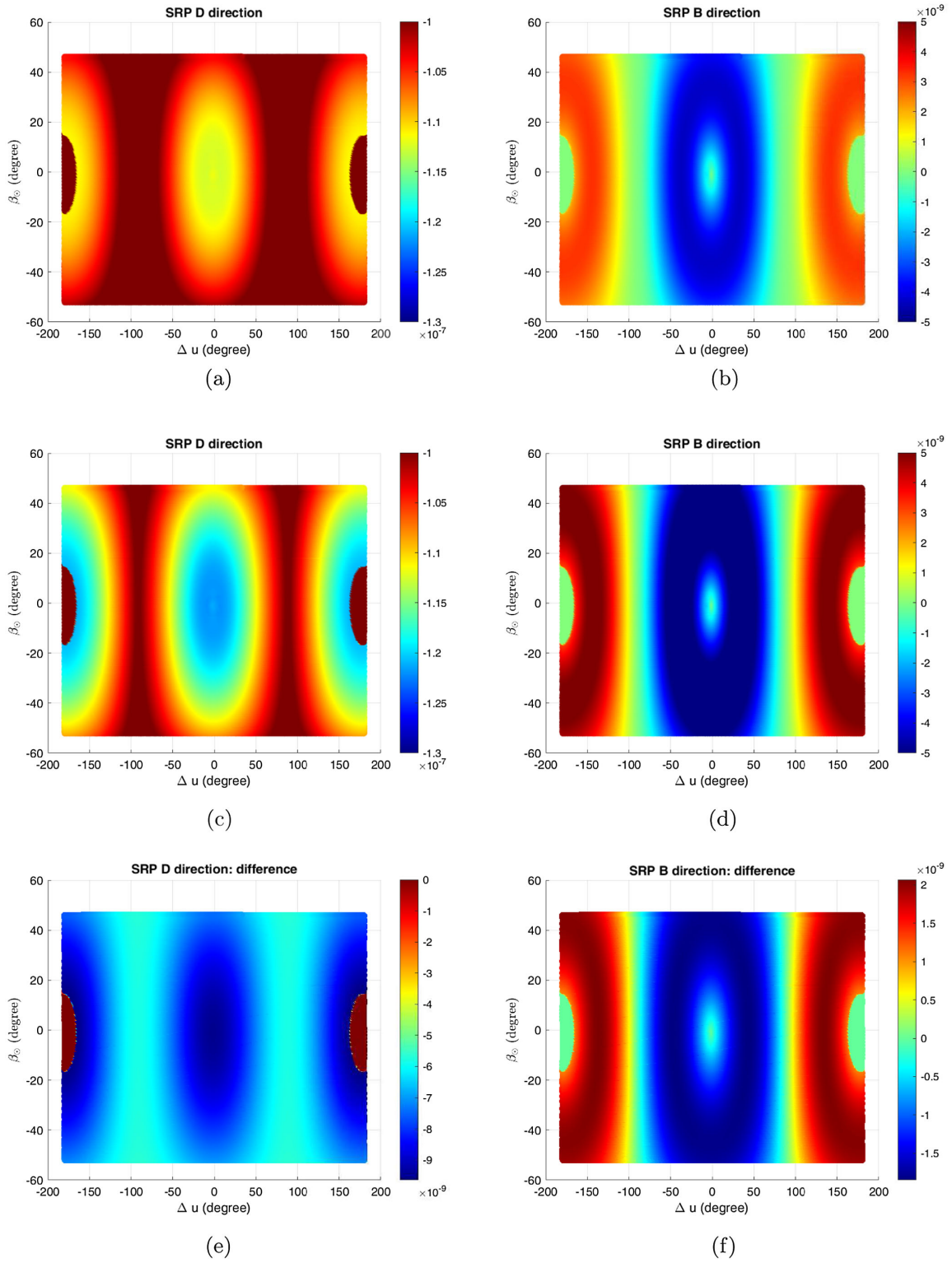


FIG. 14. GSAT0201 (E18): synoptic view of the acceleration due to direct SRP along the D and B directions. (a) GSAT0201 (E18): synoptic view of the acceleration due to direct SRP along the D direction; (b) GSAT0201 (E18): synoptic view of the acceleration due to direct SRP along the B direction; (c) GSAT0201 (E18): synoptic view of the acceleration due to direct SRP along the D direction in case of immediate thermal re-radiation; (d) GSAT0201 (E18): synoptic view of the acceleration due to direct SRP along the B direction in case of immediate thermal re-radiation; (e) GSAT0201 (E18): differences in the synoptic representation of the acceleration due to direct SRP along the D direction with and without thermal re-radiation; and (f) GSAT0201 (E18): differences in the synoptic representation of the acceleration due to direct SRP along the B direction with and without thermal re-radiation.

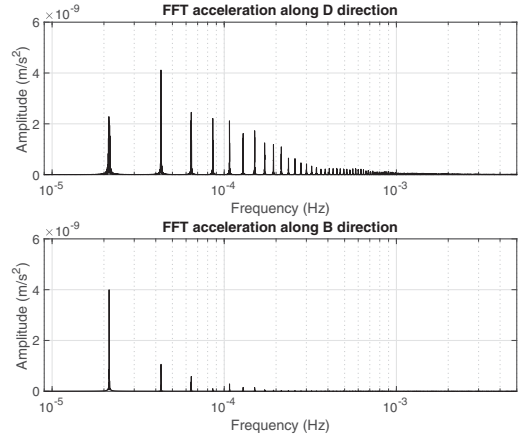


FIG. 15. GSAT0201 (E18): spectral analysis of the SRP accelerations along the D (top) and B (bottom) directions.

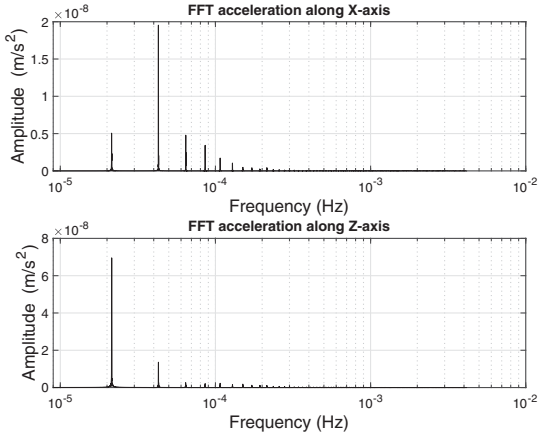


FIG. 16. GSAT0201 (E18): spectral analysis of the SRP accelerations along the X (top) and Z (bottom) directions.

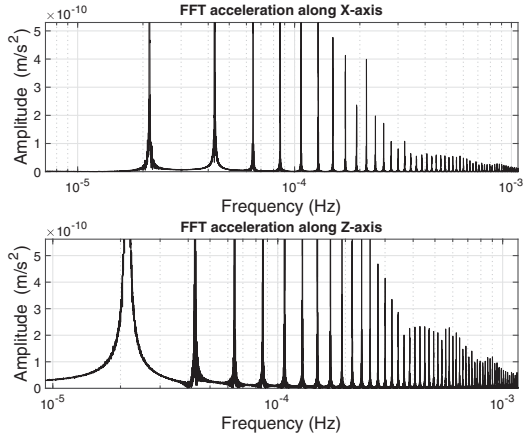


FIG. 17. GSAT0201 (E18): spectral analysis of the SRP accelerations along the X (top) and Z (bottom) directions. Particular of Fig. 16.

TABLE V. GSAT0201 (E18). Acceleration values (in units of $10^{-9}$ m/s$^2$) for the D, B, X, and Z components of the SRP for the first five spectral lines.

| Component | $f_{\mathrm{orb}}$ | $2f_{\mathrm{orb}}$ | $3f_{\mathrm{orb}}$ | $4f_{\mathrm{orb}}$ | $5f_{\mathrm{orb}}$ |
|---|---|---|---|---|---|
| D | 2.28 | 4.12 | 2.45 | 2.21 | 2.12 |
| B | 4.00 | 1.06 | 0.58 | 0.10 | 0.29 |
| X | 5.05 | 19.54 | 4.78 | 3.43 | 1.72 |
| Z | 69.53 | 13.58 | 2.62 | 2.11 | 2.30 |

an amplitude of about $6.95 \times 10^{-8}$ m/s$^2$. In the case of X-component, the line at the orbital frequency has an amplitude of about $5.0 \times 10^{-9}$ m/s$^2$, while for the Z-component the line at twice of the orbital frequency has an amplitude of about $1.36 \times 10^{-8}$ m/s$^2$.

To find accelerations with amplitude of the order of few times $10^{-10}$ m/s$^2$, comparable to the main effects of thermal origin (see Table II), periodic effects with frequency greater than $6 \times 10^{-5}$ Hz must be considered, see Fig. 17 and Table V.

Table V summarizes, for the first five spectral lines, the values of the amplitudes found for the four components of the direct SRP acceleration analyzed here.

The results obtained in terms of spectral lines are congruent with those shown in [4], although the representation is different, since these authors expressed the amplitudes as a function of the orbital revolutions and not of the frequency in Hz. The amplitudes of the different lines are slightly different in the cited paper mainly because are calculated over a different (smaller) time length.

In Fig. 18 also the long-period effects of SRP in the X and Z directions are shown. Obviously, the low-frequency effects are not as evident as the high-frequency ones, since the timespan of the analysis is not long enough to adequately resolve them.

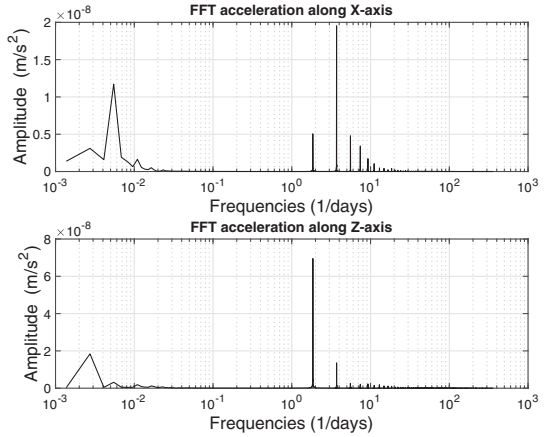


FIG. 18. GSAT0201 (E18): spectral analysis of the SRP accelerations along the X (top) and Z (bottom) directions also showing the long-period effects of direct SRP.

## IV. LONG-TERM ANALYSES: ORBITAL EFFECTS

In this section we are interested to introduce an estimate of the long-term effects on satellite orbits produced by direct solar radiation pressure on the basis of the previously introduced S-BW model. We want to underline that the BW model, although it is not a good approximation of the satellite behavior as far as short-term effects are concerned, is nevertheless useful for delineating the long-term perturbative effects of direct SRP.

This will provide us with useful information regarding some measures of fundamental physics, such as the relativistic precessions of the orbits and the consequent constraints that can be placed on some alternative theories of gravitation, i.e., alternative to general relativity in their predictions.

The most natural way to proceed in this direction is to exploit the accelerations produced by the SRP in the Gauss triad through the corresponding perturbation equations of the osculating elements. In particular, Gauss' perturbation equations describe the variations of the Keplerian elements under the action of a perturbing acceleration of any origin, i.e., due to conservative or nonconservative forces. In the following the Gauss equations for the osculating ellipse are shown [35]:

$$\frac{da}{dt} = \frac{2}{n\sqrt{1-e^2}}[T + e(T\cos f + R\sin f)] \tag{8}$$

$$\frac{de}{dt} = \frac{\sqrt{1-e^2}}{na}[R\sin f + T(\cos f + \cos E)] \tag{9}$$

$$\frac{dI}{dt} = \frac{W}{H} r\cos(\omega + f) \tag{10}$$

$$\frac{d\Omega}{dt} = \frac{W}{H\sin I} r\sin(\omega + f) \tag{11}$$

$$\frac{d\omega}{dt} = \frac{\sqrt{1-e^2}}{nae}\left[-R\cos f + T\left(\sin f + \frac{1}{\sqrt{1-e^2}}\sin E\right)\right] - \frac{d\Omega}{dt}\cos I, \tag{12}$$

where $r$ represents the satellite distance from the Earth and $H$ represents the orbital angular momentum per reduced mass of the two–body problem, while $R$, $T$, and $W$ are the components of the acceleration in the Gauss form along the radial, transversal and out-of-plane directions, respectively. In these equations the quantities $a$, $e$, $I$, $\Omega$, and $\omega$ are, respectively, the satellite's semimajor axis, eccentricity, inclination, longitude of the ascending node and argument of perigee, already introduced. The fast angular variables $f$ and $E$ are the satellite's true anomaly and eccentric anomaly, finally $n$ represents the satellite mean motion ($n = 2\pi/P$, where $P$ represents the revolution period see Table I). The essence of the method is to write the time derivatives of the parameters characterizing the perturbed satellite orbit, and then numerically integrate them in order to find the effects in the elements.

Concerning the Gauss equation for a fast variable, such as the mean anomaly $M$, we have to consider two perturbing equations in general. In fact, since the temporal variation of $M$ must be the expression of both the perturbative effects and of the mean motion along the osculating ellipse, we can introduce two fast variables $\eta$ and $\rho$, such that $M(t) = \eta + \rho$ represents the osculating mean anomaly at time $t$ with $\dot{\rho} = n$. Finally, for the time variation of these two perturbations we obtain:

$$\frac{d\eta}{dt} = R\left[\frac{\cos E}{nae(1-e^2)} - \frac{\sqrt{1-e^2}\sin f\sin E}{na} + \frac{2r}{na^2}\right] + T\left[\frac{\sqrt{1-e^2}\sin E}{nae}\left(\frac{a}{r} - 1\right) + \frac{\sqrt{1-e^2}}{na}\sin E(\cos f + \cos E)\right] \tag{13}$$

and

$$\frac{d^2\rho}{dt^2} = \dot{n} = -\frac{3}{a\sqrt{1-e^2}}[T + e(T\cos f + R\sin f)] \tag{14}$$

This approach, as explained in [35], as the advantage of introducing an element that changes "slowly," i.e., with a time derivative going to zero with the perturbative acceleration. Equations (13) and (14) are comparable in their predictions as soon as the perturbing acceleration—in particular the $T$ component—is periodic, i.e., as soon as the semimajor axis and the mean motion oscillate around an average value. Conversely, the contribution from Eq. (14) become predominant if $T$ is constant, in such a way that the changes in mean anomaly accumulate quadratically. We refer to [35] for further details and the complete mathematical derivation of Gauss perturbing equations.

Figures 19–24 show the results obtained for the variation of the six keplerian elements of GSAT0201 on the basis of our S-BW model and the Gauss perturbing equations. The units of measurement are in m/d and 1/d, respectively for the rate in the semimajor axis and in the eccentricity of the satellites, while they are in rad/d for the angular variables.

In the case of GSAT0202, only the semimajor axis behavior is shown in Fig. 19(b) since, upon first visual inspection, the results look identical for the two satellites. Of course, they are not exactly the same. The apparent overlapping of the results in the different elements arises

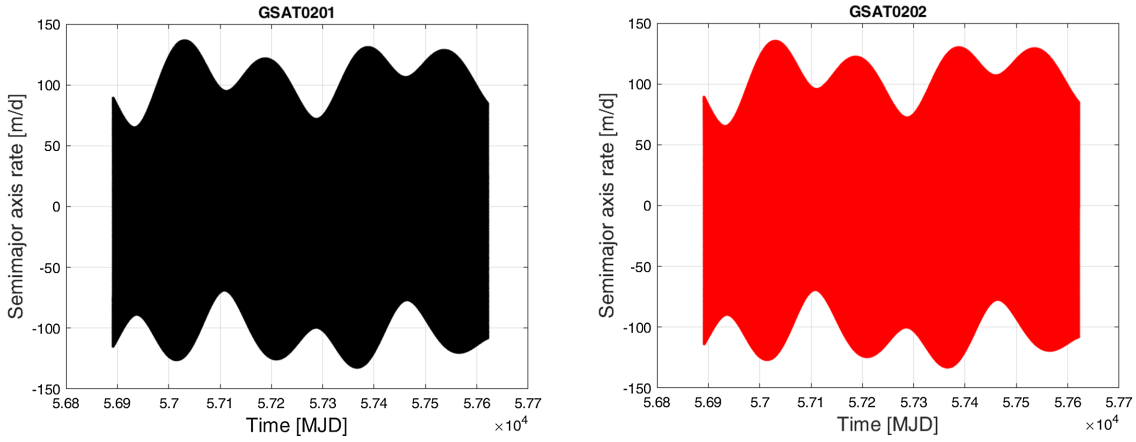


(a) (b)

FIG. 19. Long-term evolution of the semimajor axis rate of the satellites. (a) GSAT0201: long-term evolution of semi-major axis rate $\dot{a}$. (b) GSAT0202: long-term evolution of semi-major axis rate $\dot{a}$.

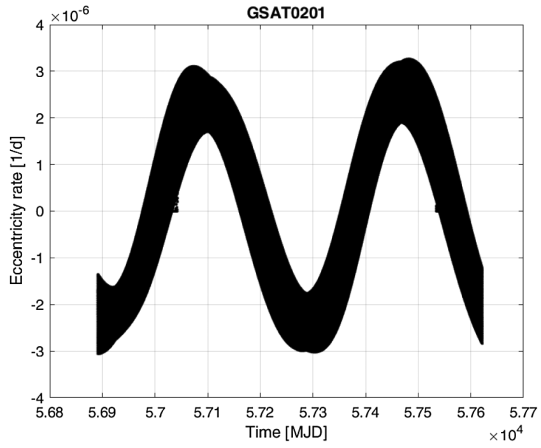


FIG. 20. GSAT0201: long-term evolution of eccentricity rate $\dot{e}$.

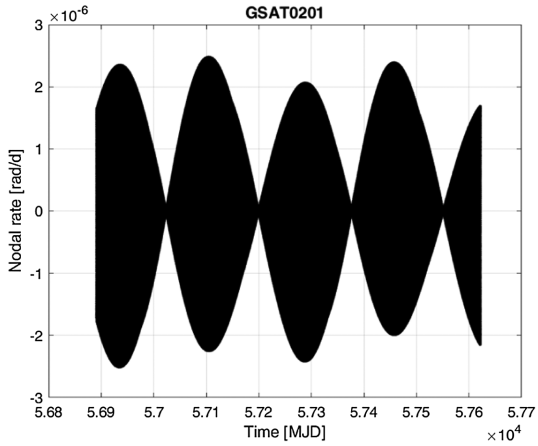


FIG. 22. GSAT0201: long-term evolution of the RAAN rate $\dot{\Omega}$.

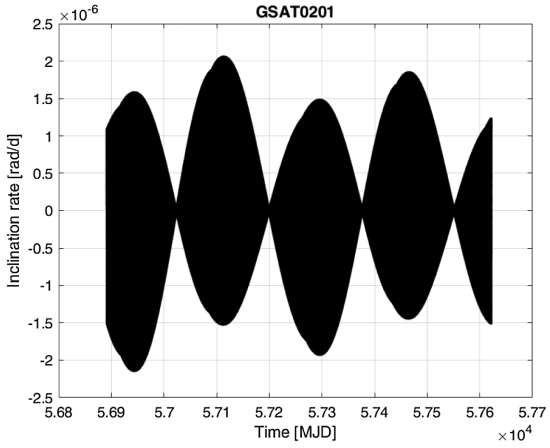


FIG. 21. GSAT0201: long-term evolution of inclination rate $\dot{I}$.

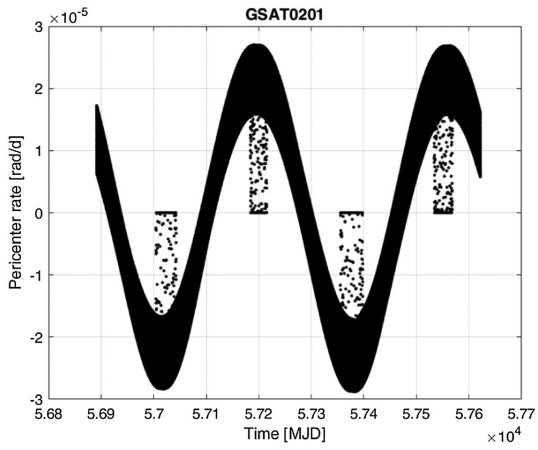


FIG. 23. GSAT0201: long-term evolution of the argument of pericenter rate $\dot{\omega}$.

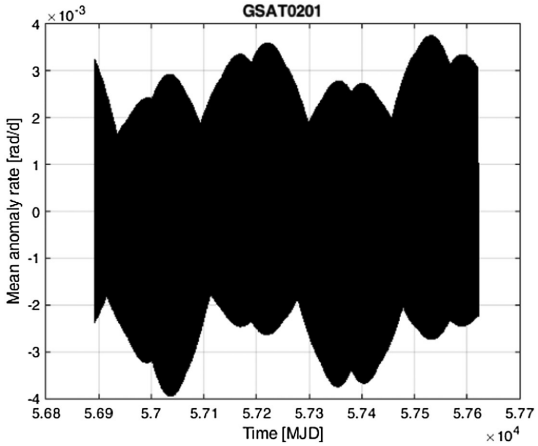


FIG. 24. GSAT0201: long-term evolution of the Mean anomaly rate in $\eta$: $\dot{\eta}$.

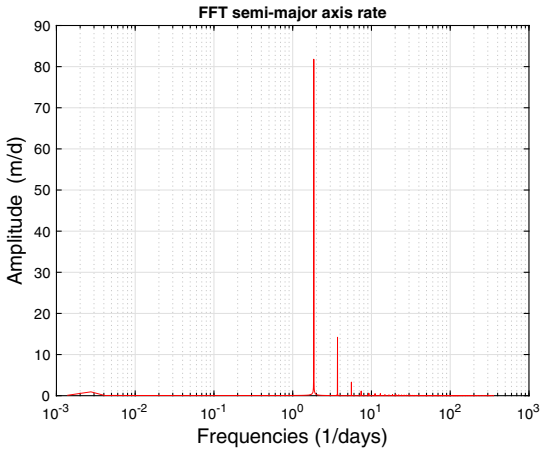


FIG. 26. GSAT0202 (E14): spectral analysis for the rate of the semimajor axis long-period effects of direct SRP.

from the fact that the orbits are very close to each other, practically with the same mean elements and very close initial conditions, see previous Tables I and IV.

The nonoverlapping of the results is evident in Fig. 25, where the evolution of the rate of the right ascension of the ascending node (RAAN) and of the rate of the argument of pericenter for the two satellites are compared over a limited time interval of some orbits. In the case of the nodal rate, the evolution is characterized by the same amplitude, but with opposite phase. Conversely, in the case of the rate of the argument of pericenter, the behavior is almost in phase but with different amplitudes.

In the case of the mean anomaly variation, see Fig. 24, we plotted the long-term behavior of $\dot{\eta}$, since the variation in $\rho$ is comparable because of the behavior of the semimajor axis rate, mainly characterized by an oscillation at the orbital frequency, see its FFT for GSAT0202 in Fig. 26.

Clearly, the short- and long-term periodic effects characterizing the rates of the different orbital elements shown in the previous figures are those found for the three components of Gaussian acceleration further modulated by the (fast and slow) angular variables $f$, $E$, and $\omega$ which enter the Gauss equations.

In the context of the gravitation measurements of the G4S_2.0 project, in particular as regards the measurement of the relativistic precessions of the orbits of the two satellites, the long-term behavior obtained for the right ascension of the ascending node and for the argument of the pericenter are interesting to be analyzed. As can be seen from Figs. 22 and 23, integer multiples of a solar year (or rather of a draconic period) contain a complete integer number of long-period oscillations, i.e., of full cycles. This implies that the unmodeled or poorly modeled effects of direct solar radiation tend to average toward zero (even if not completely) over these time intervals, consequently reducing their impact on the estimation of systematic errors.

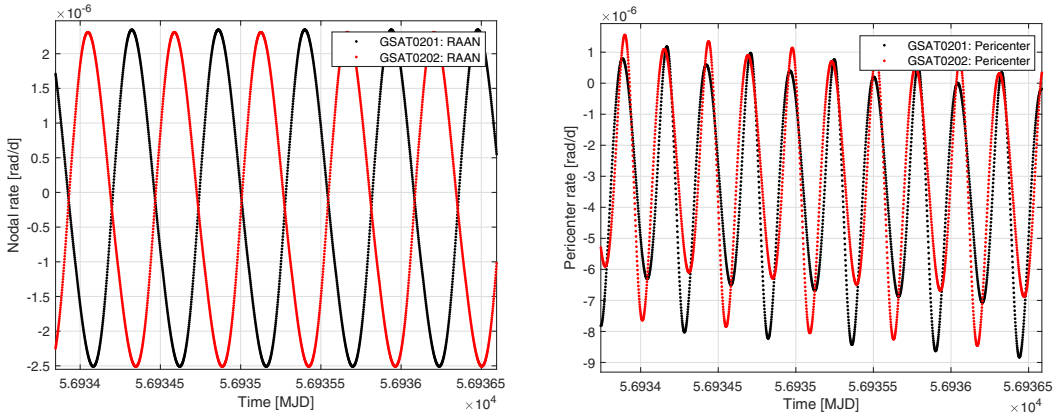


(a) (b)

FIG. 25. Differences in the long-term evolution of the RAAN rate and of the argument of pericenter rate of the satellites. (a) GSAT0201 and GSAT0202: differences in the long-term evolution of the RAAN rate $\dot{\Omega}$. (b) GSAT0201 and GSAT0202: differences in the long-term evolution of argument of pericenter rate $\dot{\omega}$.

TABLE VI. GSAT0201 (E18). Average values in rad/d (first line) and in mas/yr (second line) for the rate of the argument of pericenter $\dot{\omega}$ on different time intervals of our 2-year analysis.

| Element | First 8 months | 1st year | 2 years | 2nd year | Last 8 months |
|---|---|---|---|---|---|
| $\langle\dot{\omega}\rangle$ | $-8.698 \times 10^{-6}$ | $+1.77 \times 10^{-7}$ | $+7.0 \times 10^{-8}$ | $-3.6 \times 10^{-8}$ | $+4.396 \times 10^{-6}$ |
| $\langle\dot{\omega}\rangle$ | −655, 291 | +13, 335 | +5, 274 | −2, 712 | +331, 187 |

In Table VI, the average value we obtained for the rate of the argument of pericenter on five different time intervals of our 2-year analysis are shown. Results are provided in both rad/d and mas/yr (milli-arc second per year), where 1 mas/yr $\approx 1.3 \times 10^{-11}$ rad/d.

From the comparative analysis of this Table with Fig. 23 it is possible to obtain some useful information in view of future measurements in the field of gravitation. The average changes by about two orders of magnitude when moving from an interval of about 8 months to an interval containing a draconic period or two draconic periods. Furthermore, even over two different draconitic periods of one year, the averages are different, since the maximum positive amplitudes and the maximum negative amplitudes are different, due to the variation of the height of the Sun on the orbital plane of the satellite. These average values are huge when compared with the smallness of the relativistic precessions to be measured, see Table VII. This table shows, respectively for each satellite, the Schwarzschild (or Einstein) precession [43] on the argument of pericenter, the Lense-Thirring precession [44] on the RAAN and on the argument of pericenter, and finally the de Sitter precession [45] on the RAAN.

In reality, the values to be considered for the estimation of systematic errors are somewhat smaller than those indicated in Table VI. Primarily because the SRP will be modeled in the software used for the POD of the satellites: this would allow the average values to be reduced up to a factor of 100 in the case of the FEM. Furthermore, some of the parameters that will define our model, whether it is an improved BW compared to the current one or a FEM, can in turn be estimated thus allowing a further reduction of the systematic error to be attributed to our model.

Similar considerations apply in the case of the right ascension rate of the ascending node. In this case a direct measurement of the total relativistic effect is somewhat complex and probably unlikely, given the smallness of the relativistic precessions involved, see again Table VII.

TABLE VII. Relativistic precessions on GSAT0201 (E18) and GSAT0208 (E08) and their comparison with LAGEOS II. Units are in mas/yr.

| GR precession | GSAT0201 | GSAT0208 | LAGEOS II |
|---|---|---|---|
| $\dot{\omega}_{\rm Schw}$ | +428.63 | +362.72 | +3352.58 |
| $\dot{\Omega}_{LT}$ | +2.39 | +2.18 | +31.51 |
| $\dot{\omega}_{LT}$ | −5.15 | −3.77 | −57.33 |
| $\dot{\Omega}_{dS}$ | +17.64 | +17.64 | +17.64 |

## V. PRELIMINARY PODs AND ANALYSIS

In this section we introduce the preliminary results of the PODs we made for the GSAT0201 and GSAT0208 satellites. These analysis have been made using GEODYN II [46] for the data reduction of the satellites normal points (NPs). The modeling setup we are currently using is shown in Table VIII. It accounts for: (i) the satellite dynamics, (ii) the measurement procedure, and (iii) the reference frames transformations. In this context, our models comply, wherever possible, with the international resolutions and conventions, such as the International Astronomical Union (IAU) 2000 Resolutions [47] and the IERS Conventions (2010) [42].

Currently, for modeling the spacecraft in the POD we have applied a simple cannonball model with an average area-to-mass ratio of the Galileo FOC satellite, see Table I. The reason for this is twofold. On the one hand, we are interested in highlighting in the PODs results the improvements that are gradually obtained starting from a simple satellite model up to the final FEM, via the current S-BW model. On the other hand, as already highlighted in previous Sec. IV, for the long-term effects we expect that even a simplified model will be able to give us significant feedback, and our aim is to evaluate how good it is.

The analyzes covered the time interval from the launch date of the two satellites, see Table I, until November 25, 2022: that is, for about 8 years in the case of GSAT0201 and about 6.8 years in the case of GSAT0208. These time intervals were then divided into noncausally connected arcs of 7-day for the POD. The POD step size was 50 s. Furthermore, to overcome the current excessive simplification of the dynamic model, in particular of the non-gravitational forces, empirical accelerations in the form of constant and once-per-revolution have been introduced and adjusted to absorb part of the mismodeling [66].

In Figs. 27–29, the number of observations (NPs), the weighted root-mean-square (W-RMS) of the residuals in range and the mean of the residuals in range are plotted for each arc of the analyses.

The figures allow a first direct comparison of the results obtained from the PODs made with GEODYN II in the case of a satellite of the Galileo FOC constellation in elliptical orbit (GSAT0201, in black) compared with a satellite in nominal orbit (GSAT0208, in red). Figure 27 shows us that the

TABLE VIII. Models currently used for the POD obtained from GEODYN II. The models are grouped in gravitational perturbations, nongravitational perturbations and reference frames realizations.

| Model for | Model type | References |
|---|---|---|
| Geopotential (static) | EIGEN-GRACE02S/GGM05S | [48–50] |
| Geopotential (time-varying: even zonal harmonics) | GRACE/GRACE FO | [49,50] |
| Geopotential (time-varying: tides) | Ray GOT99.2 | [51] |
| Geopotential (time-varying: non tidal) | IERS Conventions 2010 | [42] |
| Third–body | JPL DE-403 | [52] |
| Relativistic corrections | Parametrized post-Newtonian | [47,53] |
| Direct solar radiation pressure | Cannonball | [46] |
| Earth albedo | Knocke-Rubincam | [54] |
| Earth-Yarkovsky | Rubincam | [55–57] |
| Neutral drag | JR-71/MSIS-86 | [58,59] |
| Spin | LASSOS | [60] |
| Stations position | ITRF2008/2014 | [61,62] |
| Ocean loading | Schernek and GOT99.2 tides | [46,51] |
| Earth Rotation Parameters | IERS EOP C04 | [63] |
| Nutation | IAU 2000 | [64] |
| Precession | IAU 2000 | [65] |

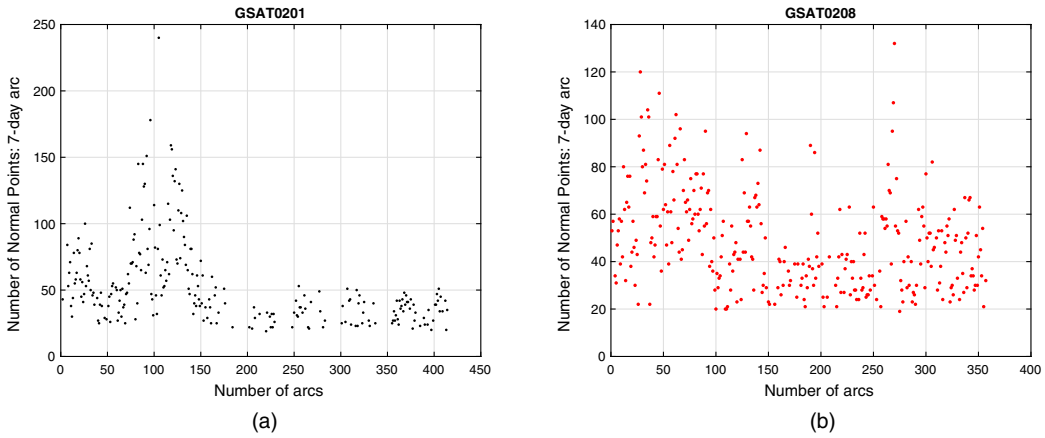


FIG. 27. Number of observations per arc. (a) GSAT0201: normal points per arc. (b) GSAT0208: normal points per arc.

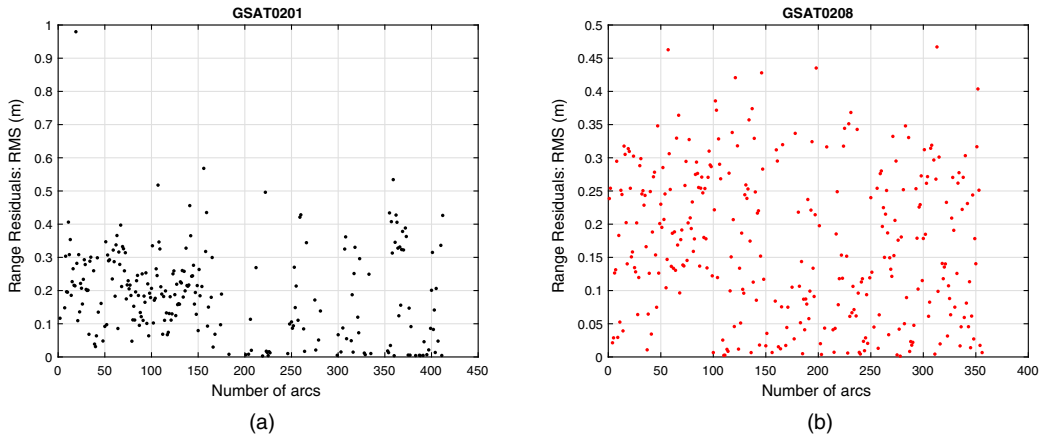


FIG. 28. W-RMS per arc of the satellites range residuals. Outliers more than three standard deviations from the mean of the W-RMS have been removed. (a) GSAT0201: weighted root-mean-square of the range residuals. (b) GSAT0208: weighted root-mean-square of the range residuals.

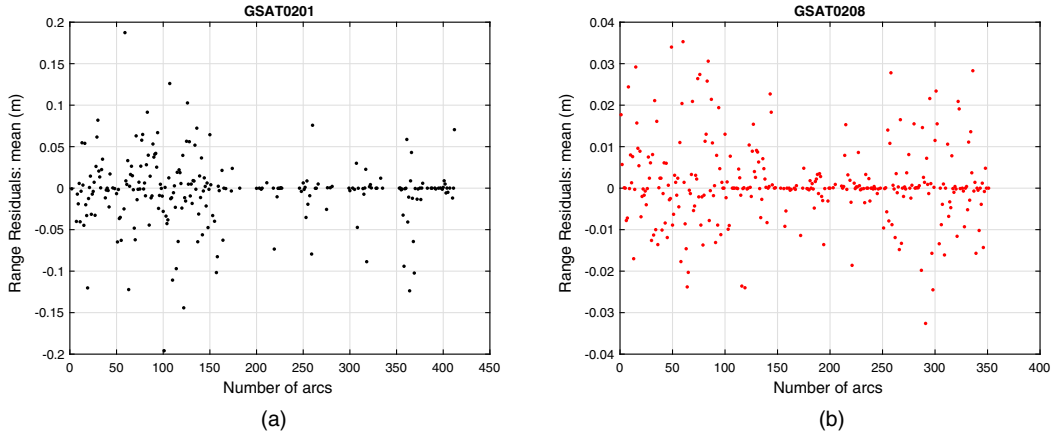


FIG. 29. Mean values per arc of the satellites range residuals. Outliers more than three standard deviations from the mean of the range residuals have been removed. (a) GSAT0201: mean of the range residuals. (b) GSAT0208: mean of the range residuals.

GSAT0208 satellite, although it was launched after GSAT0201, has been subject to a greater number of observations in the form of NPs than the satellite in elliptical orbit. In Table IX we summarize, in the case of the two satellites, the total number of normal points and their average value per year and per day. The latter value was also calculated for the 2016–2017 period of the ILRS Campaign for the Galileo gravitational Redshift Experiment with eccentric sATellites (GREAT) experiment [11,12]. As can be seen, during this 2-year period the average number of NPs for GSAT0201 is more than twice the average over the entire 8-year period considered. Conversely, the bottom line (no-GREAT) gives the average number of NPs per day after removing the 2-year period of the GREAT analysis with the dedicated SLR campaign.

Indeed, this represents a delicate aspect for some of our measurements, since in the context of G4S_2.0 we are primarily interested in the analysis of the orbits of GSAT0201 and GSAT0202 for the measurements of relativistic precessions, starting with the Schwarzschild one, the greatest of all. This scarce number of normal points for satellites in elliptical orbit is unfortunately present despite the mentioned ILRS campaign carried out for the GREAT project [67].

In Fig. 30, the NPs of the two satellites are compared as a function of time in MJD. In fact, in the period 2016 (MJD 57388)—2017 (MJD 58118), a greater number of NPs is clearly seen for the two satellites—in particular for the satellite in elliptical orbit—compared to the remaining periods, especially from 2018 onward. For this reason we asked the ILRS Central Bureau for a new dedicated observing campaign for the Galileo FOC satellites to improve the number of NPs, in view of the fundamental physics measurements of the G4S_2.0 project.

In particular, we would like to exploit the full-rate data during the penumbra transitions to improve the POD during these delicate shadow-light transitions, and vice versa, of the satellites. Additionally, full-rate data are appropriate for determining spacecraft attitude. Therefore, we should try to increase the SLR observations under these conditions, at least for the two elliptically orbiting satellites, GSAT0201 and GSAT0202. These two satellites will be used specifically for the measurement of the gravitational redshift and for the measurement of relativistic precessions. It will be anyway useful to also have an increased number of SLR

TABLE IX. Normal Points statistic for GSAT0201 and GSAT0208 on the respective time spans of the analyses performed with GEODYN II.

| Normal Points | GSAT0201 | GSAT0208 |
|---|---|---|
| Number of NPs | 13,244 | 15,249 |
| NPs/yr | 1661 | 2235 |
| NPs/d | 4.5 | 6.1 |
| NPs/d (GREAT) | 10.9 | 9 |
| NPs/d (no-GREAT) | 2.7 | 5.1 |

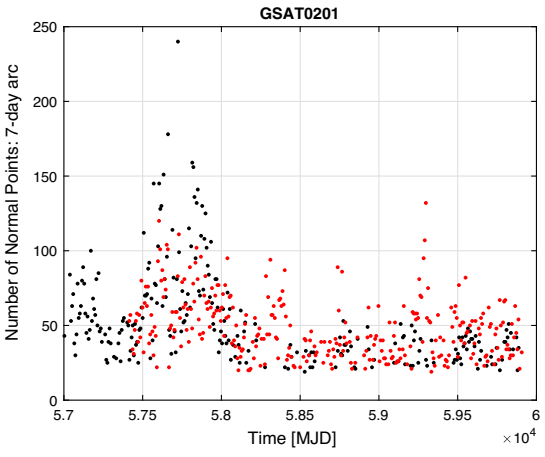


FIG. 30. GSAT0201 (E14) and GSAT0208 (E08): direct comparison of the available observations in the NPs format up to November 25, 2022.

TABLE X. GSAT0201 and GSAT0208: statistic indicators for the mean of the range residuals (RR) and for their weighted RMS on the respective time spans of the analyses performed with GEODYN II.

| GSAT0201 | Mean | Standard deviation (cm) |
|---|---|---|
| RR | −1.5 mm | 8.62 |
| W-RMS | 21.44 cm | 25.51 |
| GSAT0208 | Mean | Standard deviation (cm) |
| RR | +0.6 mm | 1.20 |
| W-RMS | 17.30 cm | 11.85 |

observations for the other Galileo's in nominal orbits, to be used for the dark matter constraints of the project.

Finally, an increased number of SLR data is important to reduce systematic errors in the measurements to be performed. Orbit modeling errors are strongly correlated to the clock solutions and SLR data are essential to characterize orbital radial errors in the IGS Analysis Centers solutions: in fact, the radial systematic errors are one to one correlated with the onboard clock solution. Since these systematic errors are mainly due to the mismodeling of the direct solar radiation pressure, it will be useful to have a campaign long enough to account for the variation of the Sun beta angle, whose period of variation (as we have seen in Sec. II A) is equal to the Draconit year, i.e., very close to 365 days.

As mentioned above, in Figs. 28 and 29 the weighted root-mean-square (W-RMS) of the residuals in range and the mean of the residuals in range are shown for each arc of the analyses. The range residuals are defined as:

$$O_i - C_i = -\sum_j \frac{\partial C_i}{\partial P_j} dP_j + dO_i, \tag{15}$$

where $O_i$ and $C_i$ are, respectively, the range observations and their computed (from the dynamical model) values, $dP_j$ represent the corrections to the vector $P$ of parameters to be estimated and, finally, $dO_i$ are the errors associated with each observation. These errors account for both the contribution from the noise in the observations as well as for the incompleteness of the mathematical model included in the software used for the orbit determination. In practice, the orbit determination is reduced to the least-squares solution of Eq. (15).

The scattering of plotted data in these two figures is a clear indicator that POD results are suboptimal due to the nonideal modeling of NGPs and, in particular, direct solar radiation pressure, here provided by a simple cannonball model. This is more evident in the case of GSAT0201 in elliptical orbit. In Table X we summarized the statistic we obtained for both the range residuals and their root-mean-square.

As can be seen the mean value of the W-RMS of the range residuals is about 20 cm in both cases (with a comparable standard deviation), when the POD of satellites in nominal orbit is usually at the level of a few cm RMS, or even less when carrier phase is used as tracking data [27]. The fact that the mean value of the residuals in range converges toward zero (close to about ±1 mm)—and this is well highlighted in the histograms of the range residuals of the two satellites in Fig. 31—should not mislead.

This is due to the use of the previously mentioned empirical accelerations, which assume large values after data reduction. This is shown below in Figs. 32–34.

These are general acceleration terms added to the equations of motion, and are aimed at modeling and/or absorbing otherwise unknown small effects which may be relevant for the dynamics. In GEODYN II, these acceleration are decomposed in the three Gauss directions under the general form:

$$a(t) = a_0(t) + a_c(t)\cos(\omega(t) + f(t)) + a_s(t)\sin(\omega(t) + f(t)), \tag{16}$$

where the amplitudes $a_c$ and $a_s$ define the terms of acceleration at orbital frequency. In these figures we plotted

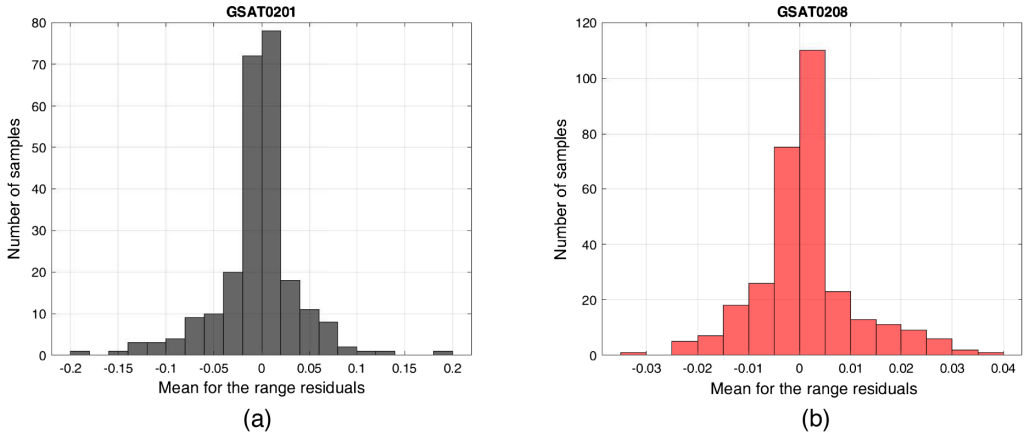


FIG. 31. Histogram of the range residuals of Fig. 29. (a) GSAT0201: histogram of the range residuals of Fig. 29(a). (b) GSAT0208: histogram of the range residuals of Fig. 29(b).

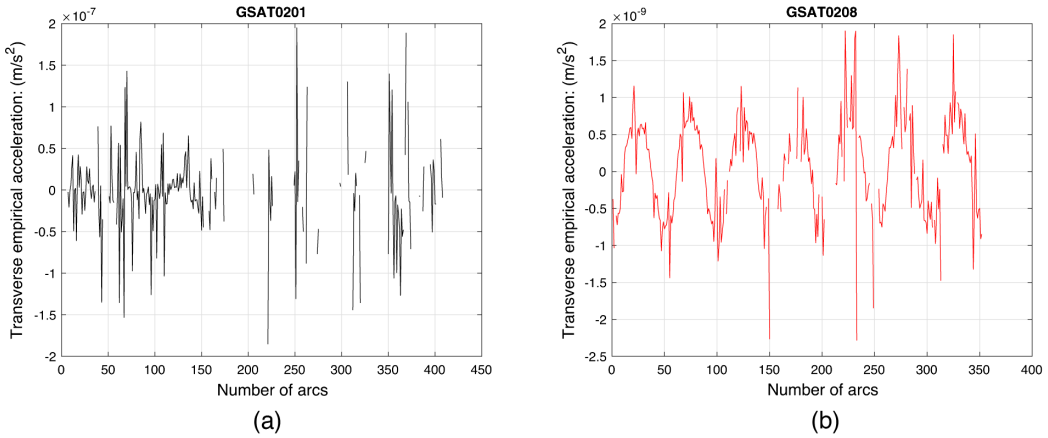


FIG. 32. Empirical transverse (constant component) acceleration (m/s$^2$), estimated for each arc of the POD. Outliers more than three standard deviations from the mean of the acceleration values have been removed. (a) GSAT0201: empirical transverse acceleration per arc: $T_0$ constant acceleration. (b) GSAT0208: empirical transverse acceleration per arc: $T_0$ constant acceleration.

the transverse acceleration for the two satellite, the most important in defining the shape of the orbit, as can be seen from Gauss equations (8) and (9) for the satellite semimajor axis and eccentricity.

From these figures it is once again evident the scarcity of the NPs of the satellites, in particular of GSAT0201, clearly evident in the arcs in which the data reduction has not been successful (holes in the data). Other information obtained from the plots is the high value of the estimated arc-by-arc amplitudes for the transverse acceleration in the PODs of the two satellites. This is evident from the empirical acceleration terms at orbital frequency, i.e., from the once-per-rev terms $T_c$ and $T_s$, which generally assume amplitudes of the order of some $10^{-7}$ m/s$^2$, i.e., more than one order of magnitude larger than the estimated peak values through our S-BW model, see Sec. III A 2. The situation is better in the case of the constant term for the satellite GSAT0208, whose maximum amplitudes are two orders of magnitudes smaller than those estimated for the satellite in elliptical orbit. Furthermore, the long-term trend is also well defined, with a periodicity close to the annual one.

However, in spite of the picture just described, which is not too comforting, if we look at the long-term effects on the orbital elements provided by the cannonball model, the results are somewhat more interesting for our purposes. This will be analyzed in next section.

### A. PODs long-term effects: GSAT0201

Figures from 35 to 39 show the results obtained for the long-term evolution of the keplerian elements of GSAT0201 in elliptical orbit. In Sec. II of the Supplemental Material [39] are reported the results obtained in the case of GSAT0208 in nominal orbit. Specifically, the plotted values represent the adjustment of the state-vector at the start of

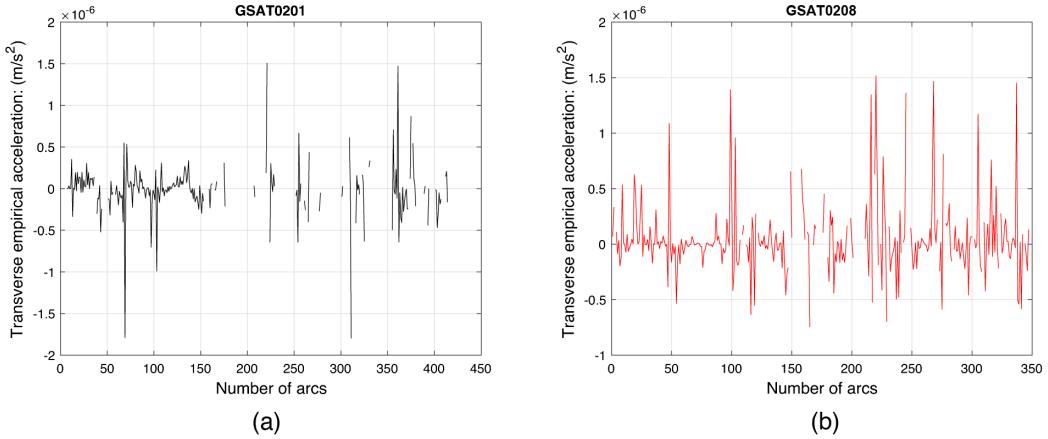


FIG. 33. Empirical transverse (cosine component) acceleration (m/s$^2$), estimated for each arc of the POD. Outliers more than three standard deviations from the mean of the acceleration values have been removed. (a) GSAT0201: empirical transverse acceleration per arc: $T_c$ amplitude of the cosine term. (b) GSAT0208: empirical transverse acceleration per arc: $T_c$ amplitude of the cosine term.

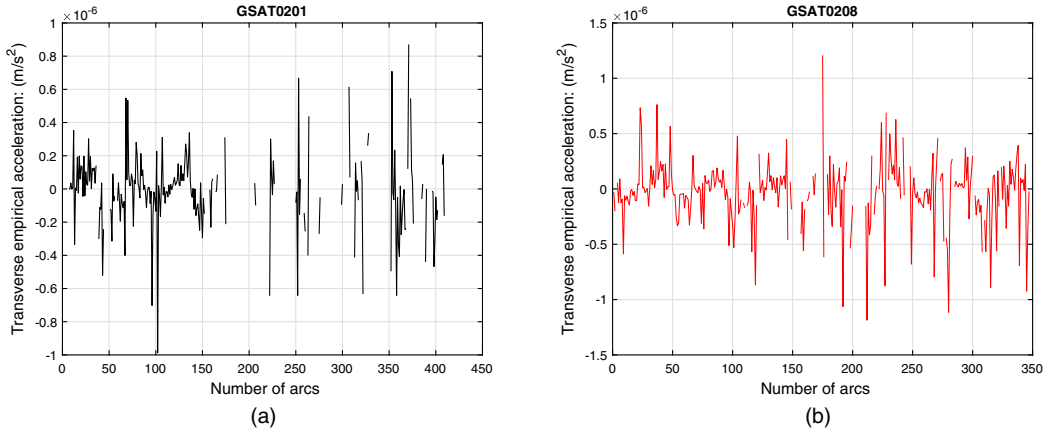


FIG. 34. Empirical transverse (sine component) acceleration (m/s$^2$), estimated for each arc of the POD. Outliers more than three standard deviations from the mean of the acceleration values have been removed. (a) GSAT0201: empirical transverse acceleration per arc: $T_s$ amplitude of the sine term. (b) GSAT0208: empirical transverse acceleration per arc: $T_s$ amplitude of the sine term.

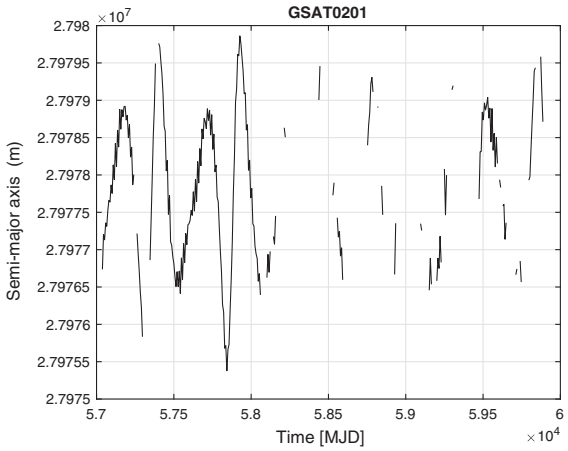


FIG. 35. GEODYN II POD of GSAT0201: long-term evolution of the semimajor-axis.

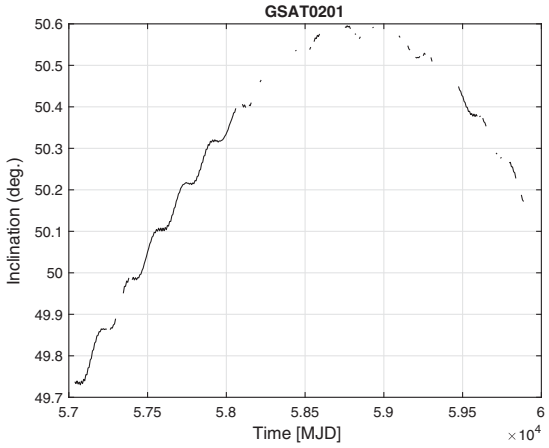


FIG. 37. GEODYN II POD of GSAT0201: long-term evolution of the inclination.

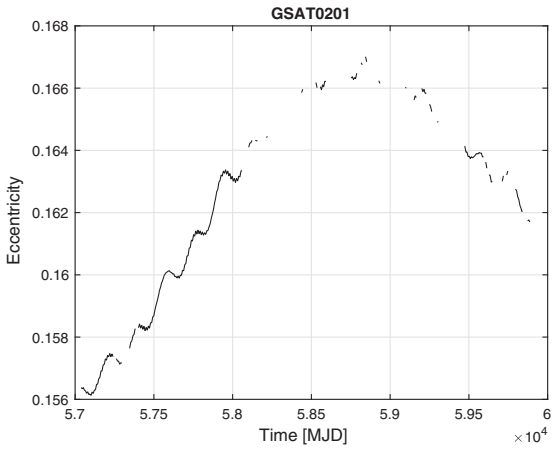


FIG. 36. GEODYN II POD of GSAT0201: long-term evolution of the eccentricity.

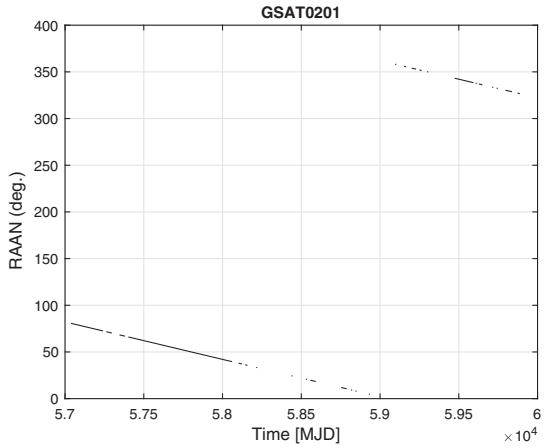


FIG. 38. GEODYN II POD of GSAT0201: long-term evolution of the right ascension of the ascending node.

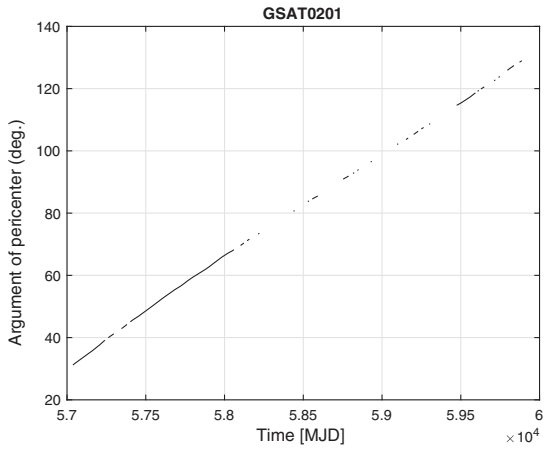


FIG. 39. GEODYN II POD of GSAT0201: long-term evolution of the argument of pericenter.

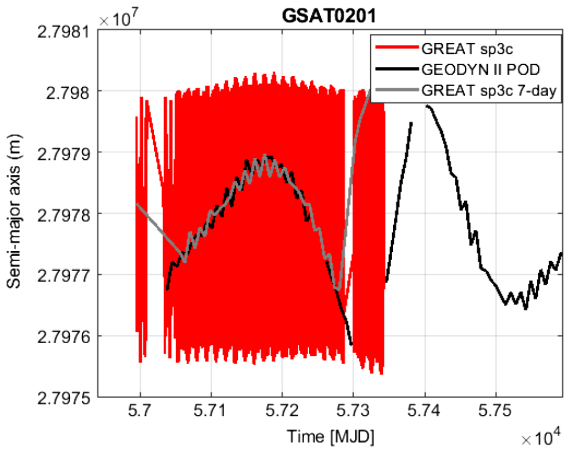


FIG. 40. Comparison between GEODYN II POD (black) and GREAT sp3c precise orbit (red): long-term evolution of the semimajor axis of GSAT0201.

each 7-day arc to best fit the available tracking observations of GSAT0201.

As said, the models implemented are those of Table VIII. For the Earth's background gravitational field we used EIGEN-GRACE02S [48] up to degree and order 30. The initial (a-priori) state-vector for the satellites was obtained from their Two Line Elements (TLE) as provided by NORAD (see [68]).

As we can deduce from these figures, in the case of GSAT0201 the long-term evolution of the orbital elements is different than that of GSAT0208 (see Figs. 7–11 in the Supplemental Material [39]). This is primarily due to the eccentricity of the orbit. In particular, an eccentricity significantly different from zero is responsible for further long- and (also short-) term perturbation effects, starting with the Earth's gravitational field [69].

In the following we want to compare the results of our PODs with those obtainable from the precise orbits obtained from the IGS analysis centres. In particular, we will compare our PODs with the precise orbits obtained by ESOC for the previous GREAT experiment. The precise orbits, already introduced in Sec. III, are distributed according to the sp3c format. These orbits are the highest quality IGS solutions and consists of daily files produced on a weekly basis.

The results of the comparison in the case of GSAT0201 and GSAT0208 are shown in Figs. 40–44 below and in Figs. 12–16 in the Supplemental Material [39]. Results are shown for the semimajor axis, eccentricity, inclination, right ascension of the ascending node, and argument of pericenter of the satellites. As can be seen from practically all the figures, the agreement on the long-term behavior of the orbits obtained with GEODYN II, based on a simple cannonball model, with those obtained from the sp3c files is quite good. In the case of GREAT, the precise orbits were obtained from ESA's NAPEOS orbital determination code [70], probably exploiting the dynamic models for nongravitational forces developed within this project.

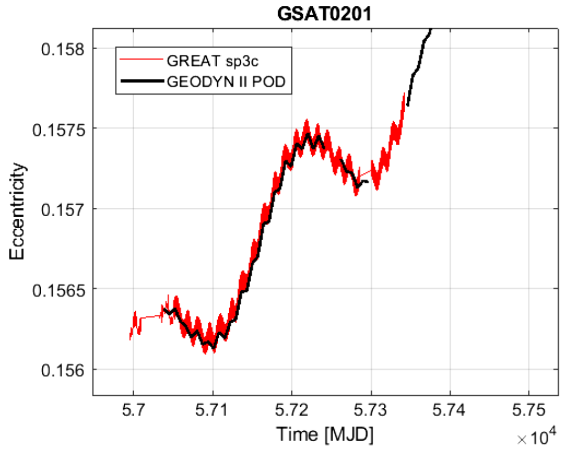


FIG. 41. Comparison between GEODYN II POD (black) and GREAT sp3c precise orbit (red): long-term evolution of the eccentricity of GSAT0201.

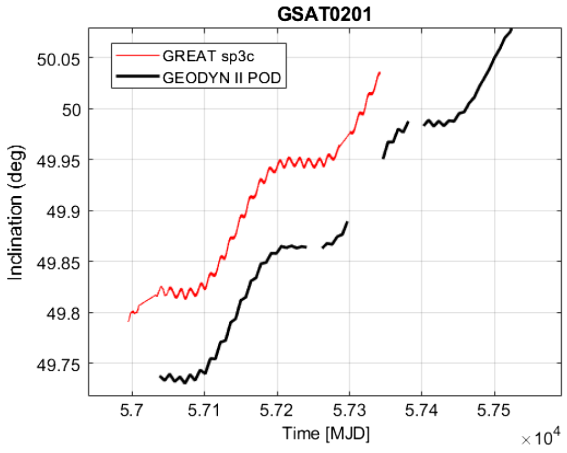


FIG. 42. Comparison between GEODYN II POD (black) and GREAT sp3c precise orbit (red): long-term evolution of the inclination of GSAT0201.

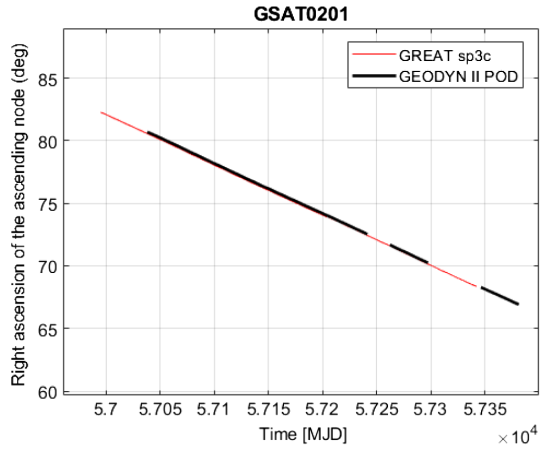


FIG. 43. Comparison between GEODYN II POD (black) and GREAT sp3c precise orbit (red): long-term evolution of the RAAN of GSAT0201.

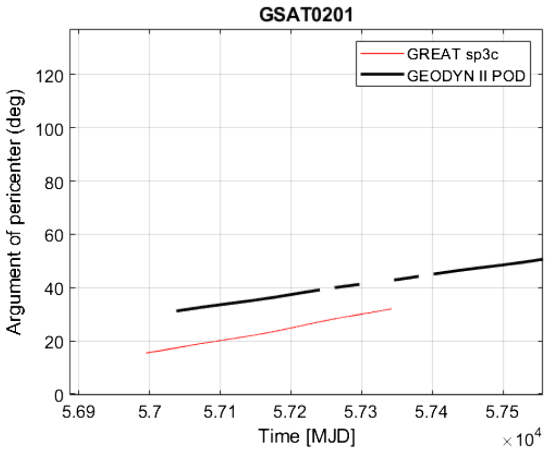


FIG. 44. Comparison between GEODYN II POD (black) and GREAT sp3c precise orbit (red): long-term evolution of the argument of pericenter of GSAT0201.

In both cases, GEODYN II vs GREAT sp3c, the osculating keplerian elements are plotted. One difference lies in the sampling time of the plotted data: 7 days in the case of the POD made with GEODYN II and 300 s in the case of the POD made by ESOC with NAPEOS. This difference is particularly evident in the case of the semimajor axis of the orbit of the two satellites considered, but less so in the other cases. For this Keplerian element we plotted the GREAT data sampled every 7 days (gray line). Even in this case the agreement is notable. For some quantities, it was preferred to plot the cumulative sum of the results obtained, as in the case of the right ascension of the ascending node of the two satellites or of the argument of the pericenter in the case of GSAT0201.

In order to begin comparing our POD results with those provided at the high frequencies of the precise orbits obtained by GREAT, we need to reduce the length of our arc and replace the cannonball model with more sophisticated models, as already anticipated, starting with the S-BW model.

However, the results obtained with the current approximation are nonetheless encouraging as regards the measurement of relativistic precessions, linked to the secular effects produced by general relativity (GR)—or by other theories of gravitation (alternatives to GR)—on the right ascension of the ascending node of the orbit and, in particular, on the argument of the pericenter of the satellites. This aspect will be further investigated in the following subsection.

The agreement is remarkable also in the case of the eccentricity of the satellites, as well as for their inclination: the differences are in the values of the initial conditions, in any case less than 0.05 degrees. The extrapolation of the initial condition from the orbits of GREAT is sometimes not easy, as in the case of the argument of pericenter of GSAT0201 but, above all, in the case of the mean anomaly of the satellites, i.e., in the case of a rapidly varying element.

These results give us a clear indication of the possibility of determining, with GEODYN II, the effects of relativistic precessions on the orbit of the Galileo FOC satellites even in the case in which the dynamic model of the satellite is not sophisticated enough, as regards the nongravitational effects. Of course it is necessary to have enough laser observations to ensure state vector convergence in the data reduction process. In the next subsection we will give a first assessment of these aspects in the case of the orbital residuals of GSAT0201.

### B. Orbit residuals in the Keplerian elements

In the following, from Figs. 45 to 50, we show the results for the residuals we obtained from the Keplerian elements of GSAT0201 after a second POD performed by GEODYN II, different from that described in Secs. V and V A. The units of measure for angular quantities are now milliarcsec (mas) per day and not rad/d, as in previous plots.

The two main differences lie in not having modeled general relativity and in not having estimated the empirical accelerations in the POD. This is a correct way, although not the only, to proceed to derive gravitational effects from the analysis of satellite orbital residuals. The model for GEODYN II relativistic corrections refers to the parametrized post-Newtonian (PPN) formalism [71–73] according to the formulation described in [53]. Of course, in this particular case of preliminary POD, the relativistic effects are completely masked by the imperfections of the dynamical model we have used.

The plotted residuals have been determined with the method described in [74] exploiting the difference between the satellite's state-vector estimated by GEODYN II at the beginning of each arc of the POD and the propagated value of the (estimated) state-vector of the previous arc at the same epoch. Since the residuals were obtained by

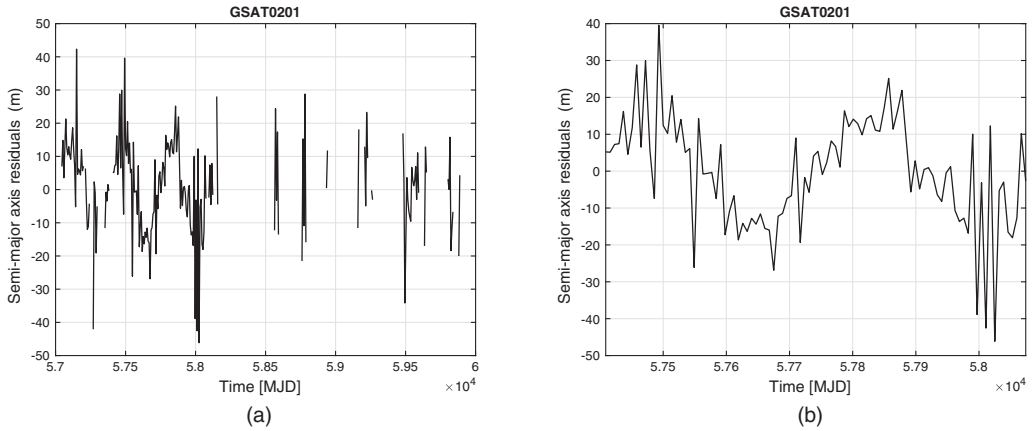


FIG. 45. GSAT0201: residuals on 7-day of the satellite's semimajor axis. (a) GSAT0201: long-term evolution of the satellite's semi-major axis residuals over the entire analysis period. (b) GSAT0201: long-term evolution of the satellite's semi-major axis residuals in the period 2016–2017.

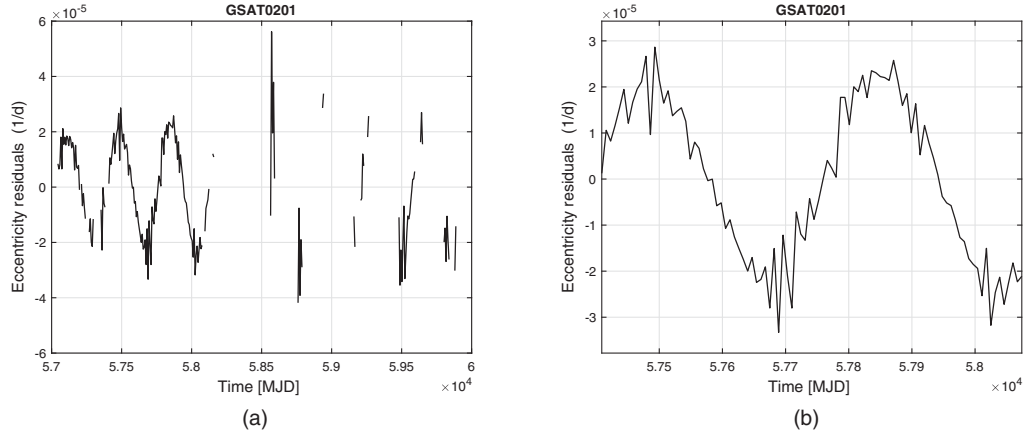


FIG. 46. GSAT0201: residuals on 7-day of the satellite's eccentricity. (a) GSAT0201: long-term evolution of the satellite's eccentricity residuals over the entire analysis period. (b) GSAT0201: long-term evolution of the satellite's eccentricity residuals in the period 2016–2017.

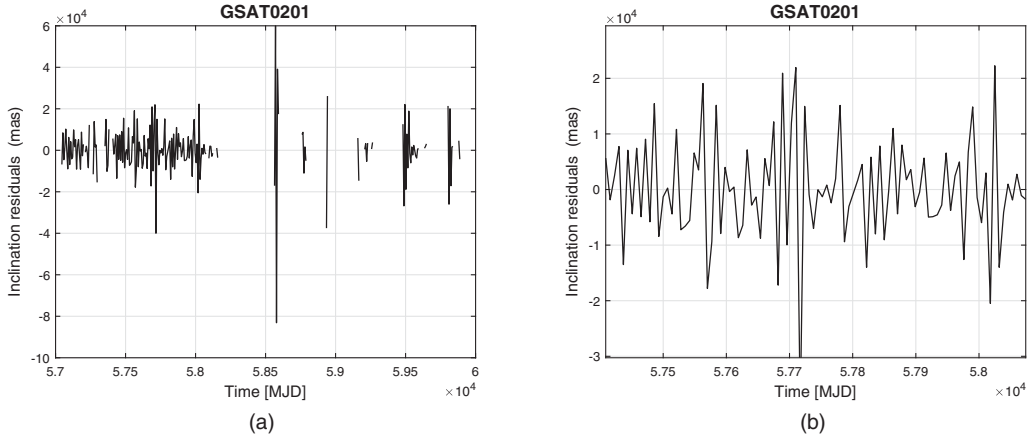


FIG. 47. GSAT0201: residuals on 7-day of the satellite's inclination. (a) GSAT0201: long-term evolution of the satellite's inclination residuals over the entire analysis period. (b) GSAT0201: long-term evolution of the satellite's inclination residuals in the period 2016–2017.

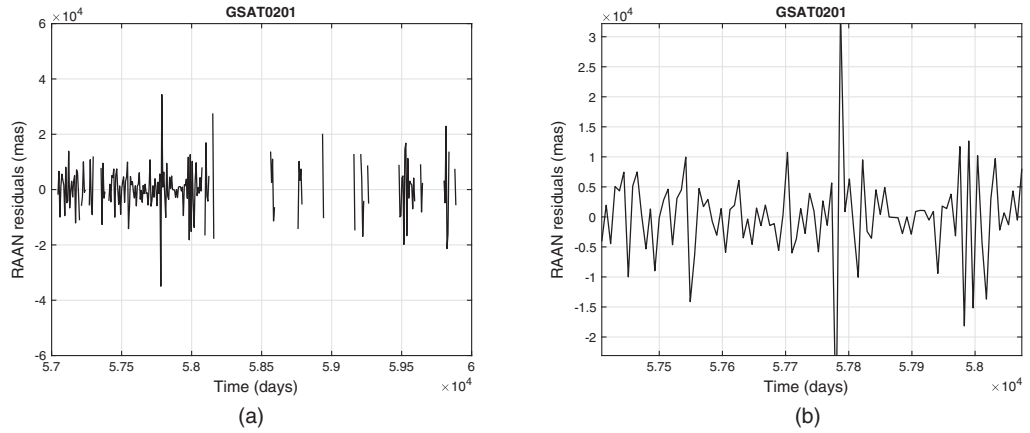


FIG. 48. GSAT0201: residuals on 7-day of the satellite's RAAN. (a) GSAT0201: long-term evolution of the satellite's RAAN residuals over the entire analysis period. (b) GSAT0201: long-term evolution of the satellite's RAAN residuals in the period 2016–2017.

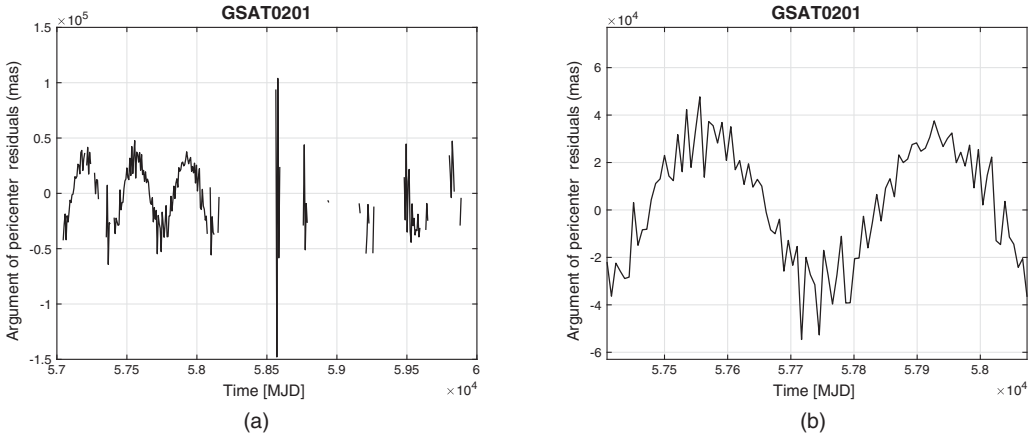


FIG. 49. GSAT0201: residuals on 7-day of the satellite's argument of pericenter. (a) GSAT0201: long-term evolution of the satellite's argument of pericenter residuals over the entire analysis period. (b) GSAT0201: long-term evolution of the satellite's argument of pericenter residuals in the period 2016–2017.

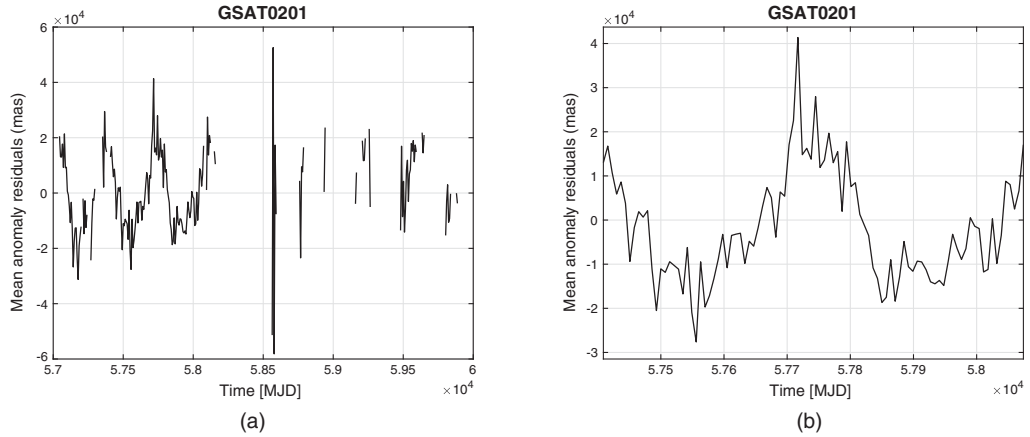


FIG. 50. GSAT0201: residuals on 7-day of the satellite's mean anomaly. (a) GSAT0201: long-term evolution of the satellite's mean anomaly residuals over the entire analysis period. (b) GSAT0201: long-term evolution of the satellite's mean anomaly residuals in the period 2016–2017.

propagating the state vector along the length of each arc, they represent, strictly speaking, the residuals in the rate of the orbital elements, more precisely their variation over 7 days.

For each figure, the plot on the left shows the residuals over the entire analysis period, i.e., over about 8 years, while the plot on the right shows the residuals we obtained over the 2-year period considered by the GREAT experiment: 2016–2017. The residuals plotted over the entire period clearly show the numerous gaps due to the nonconvergence of the state-vector during the data reduction because of the scarcity of normal points for this satellite. This was already highlighted in the previous sections. On the contrary, the residuals obtained in the period 2016–2017 do not show any discontinuity, confirming the success of the observational campaign carried out by the ILRS stations in favor of the GREAT experiment in the case of the two satellites in elliptical orbit, see previous Table IX.

As can be seen, most of the figures indicate, in the various orbital residuals, the presence of nonmodeled effects with an annual periodicity. This is less evident in the residuals in inclination and in the right ascension of the ascending node, but it is well evident in all other cases. This is a clear indication of the poor modeling of direct solar radiation for Galileo FOCs in the case of the cannonball model, which on the contrary is a good approximation in the case of passive geodetic satellites, such as LAGEOS [75].

This is indirectly confirmed in Figs. 51 and 52, where the residuals in the eccentricity rate and in the argument of pericenter rate, rescaled per day, are compared with the predictions of our S-BW model presented in Sec. IV (Figs. 20 and 23) and computed on a 4 years period. The S-BW model is in this case able to explain the quasi totality of the residuals currently determined with the POD based on the cannonball model, in particular the annual oscillation.

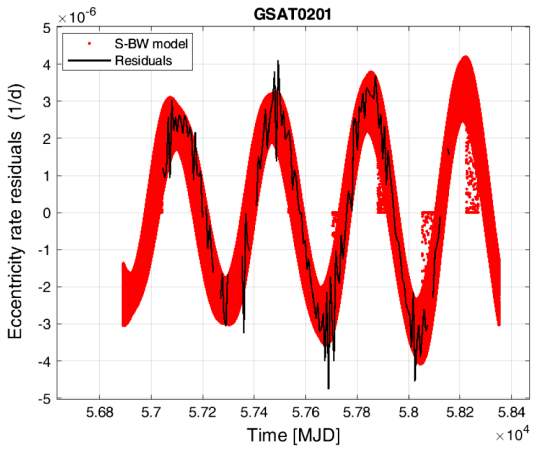


FIG. 51. GSAT0201: direct comparison of the eccentricity rate residuals with the corresponding prediction of the S-BW model on a 4-year timespan.

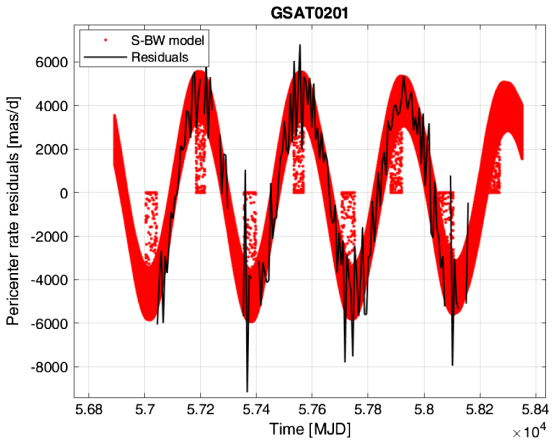


FIG. 52. GSAT0201: direct comparison of the argument of pericenter rate residuals with the corresponding prediction of the S-BW model on a 4-year timespan.

These results are remarkable and very important in view of the possibility of extracting the measure of relativistic precessions from the analysis of the orbital residuals of the Galileo FOC satellites.

## VI. CONSIDERATIONS IN VIEW OF THE GR MEASUREMENTS

In this section, we will try to summarize, and briefly discuss, the results we have obtained from the analyzes described in this work in the perspective of the next fundamental physics measurements of the G4S_2.0 project.

The question to ask is how much the model for the nongravitational perturbations of the Galileo FOC satellites, and more generally the overall dynamic model of the satellites, needs to be improved in order to achieve reliable measurements for the project's gravitational measurements? Obviously it is not easy to give a clear answer to this question at this stage of G4S.0 activities.

In the following we will restrict our considerations to the measurement of relativistic precessions which, in our planning of the various activities and measurements, should be obtained from the PODs made with the GEODYN II software.

Naturally, the level currently achieved for modeling nonconservative forces and, in particular, direct solar radiation pressure, is not sufficient for a direct measurement of relativistic precessions. For example, in the case of the relativistic precession of the argument of pericenter of GSAT0201—given by the sum of the Schwarzschild and the Lense-Thirring precessions, equal to approximately 423.5 mas/yr (see Table VII)—the result should be extracted, for instance, from the average value of the pericenter rate residuals reported in Fig. 49 or 52.

Unfortunately, both the long-term annual oscillation that characterizes the residuals in the rate of the argument of pericenter of the satellite, and the shorter-term ones

superimposed on it, provide an average value that completely masks the prediction provided by GR. Figure 52 shows implicitly that the inclusion of the S-BW model for the satellite in the POD will be able to largely absorb the long-term annual oscillation, but the higher frequency variations shown in the residuals in the pericentric rate will not be certainly absorbed.

These considerations are confirmed by the results of the preliminary activities we have undertaken by including the accelerations obtained with the S-BW model (replacing the cannonball model) in the dynamic model of GEODYN II. This result was achieved by providing two external files to GEODYN II, in binary format, one for the acceleration produced by the SRP on the box-wing model of the satellite and one for the corresponding attitude of the satellite according to the law introduced in Sec. II A.

Figure 53 provides the results for the residuals of the eccentricity rate and the argument of pericenter rate (in red) for GSAT0201 obtained using the S-BW model accelerations, compared to previous residuals obtained with the cannonball model (in black).

As can be seen, the improvements in residuals reduction are significant: about a factor of 20, or greater, in the maximum amplitude for the eccentricity rate and about a factor of 3 smaller in amplitude in the case of the argument of pericenter rate. However, these improvements are not sufficient to "easily" allow the extraction of relativistic precessions. Indeed, the new residuals in the rate of the argument of pericenter argument are still characterized by a long-term oscillation with annual periodicity, in addition to the expected high-frequency oscillations. From the new analyses, which will be the subject of a dedicated work, we have preliminarily estimated that the residual annual oscillation is due to a transversal acceleration of such periodicity and maximum amplitude of the order of $1.5 \times 10^{-8}$ m/s$^2$.

Consequently, as highlighted in previous Secs. III and IV, it will be necessary to further improve the model of the spacecraft to be used for calculating the effects of solar radiation pressure. The first step will be to achieve an improved box-wing model based on a more detailed characterization of the optical properties of the satellite face that constantly looks toward the ground. Then, as a second step, proceed further toward the improvement of the FEM model introduced in Paper I.

Only after these improvements in the SRP model, which can be estimated approximately to be a factor of 100 or 200 in the orbital residuals compared to the cannonball model, will it make physical sense to take into account the perturbative effects due to the albedo and infrared radiation of terrestrial origin.

For instance, the mean value of the residuals of Fig. 53(b) in the case of the S-BW model, is about 30 times greater than the prediction of GR for the combined Schwarzschild plus Lense-Thirring precession (and about 300 times greater in the case of the cannonball model). This difference compared to the expected value according to GR, although conspicuous, is not to be considered as an insurmountable obstacle and which consequently makes the measurement of relativistic precession impossible.

This is for a series of reasons linked, not only to the further development of the perturbative model (here we have the virtuous example of what the GREAT project has done in the case of the new measurement of gravitational redshift), but also to the different modalities with which the relativistic precession can be extracted from the different orbital residuals.

What the residuals in the various orbital elements show is not simply noise superimposed on the relativistic effects to be measured but, mainly, other effects not modeled or poorly modeled in the dynamic model and primarily of a periodic nature. Therefore, by integrating the residuals in the rate of the orbital elements, as for example in the case of

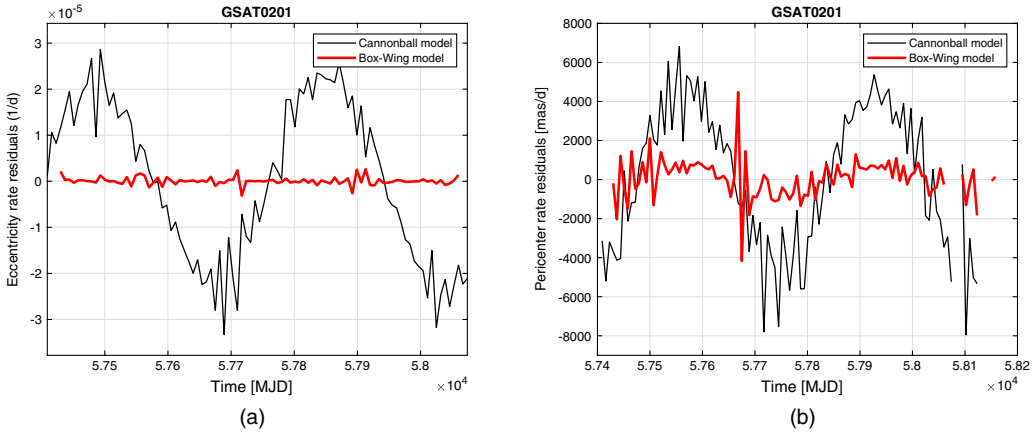


FIG. 53. GSAT0201 cannonball model vs S-BW model: residuals on 7-day of the satellite's eccentricity and argument of pericenter rates. (a) GSAT0201: long-term evolution of the satellite's eccentricity rate over the 2-year of the GREAT analysis (2016–2017). (b) GSAT0201: long-term evolution of the satellite's pericenter rate residuals over the 2-year of the GREAT analysis (2016–2017).

the rate of the argument of pericenter, we will obtain that the periodic effects integrate and remain periodic and overlap with the linear trend of a relativistic nature. The integration process also acts as a filter, hence "mitigating" the effects on the pericenter rate due to higher frequency periodic oscillations. The measurement of the slope will therefore provide the relativistic precession sought, i.e., what was before the integration in the average of the rate of the orbital element, now is in the slope of the element itself.

Of course, it is important that the time step of the analysis is long enough to include an integral number of (possible) unmodeled long-term periodic effects, which then average their effect on the mean of the residuals, or the slope of the integrated residuals, to zero. As regards the possible lack of normal points for the satellites, the measurement of relativistic precessions can still be attempted over a long time span by means of the statistical analysis used in [76].

## VII. CONCLUSIONS AND RECOMMENDATIONS

We presented some of the ongoing activities at the IAPS/INAF institute in Rome within the G4S_2.0 project in fundamental physics funded by the Italian Space Agency (ASI). These activities concern, on the one hand, the development of new models to take into account the nongravitational forces acting on the satellites of the Galileo FOC constellation of the European Space Agency (ESA), on the other, the determination of the orbit of the satellites by means of a least-square fit of the laser-ranged data (of each spacecraft) provided by the ILRS through the SLR technique.

As far as the models are concerned, as a preliminary to the finite element model of the satellite we are developing, we have introduced a box-wing model built on the basis of the metadata provided by ESA (Sec. III and Paper 1). The model has been applied to take into account the perturbation produced by direct solar radiation pressure, the largest among all the perturbations produced by nonconservative forces. The model differs in part from those reported in the literature of GNSS satellites in that the visible solar radiation absorbed by the different surfaces that make up the satellite is not modeled, in terms of its instantaneous reemission. This effect will in fact be treated more properly under the perturbations linked to the effects of thermal thrust. Conversely, and contrary to the models reported in the literature, the complete law on the complex attitude of the satellite was implemented on the basis of the information provided by ESA in its twofold form: "nominal" and "modified" (Sec. II A). In this context, we have highlighted some differences that arise in applying the attitude law to satellites in nominal orbit—or almost circular orbit (GSAT0208), for which it was built—with its application to satellites in elliptical orbit (GSAT0201). The box-wing model was used to calculate the accelerations produced by solar radiation on the different surfaces of the satellites. The accelerations have been provided in different representations—in the time domain, in a synoptic view and in the frequency domain—to highlight their different usefulness for our purposes (Sec. III A and Sec. I of the Supplemental Material [39]). Subsequently, the accelerations in the Gauss reference system were exploited to determine the corresponding effects on the Keplerian elements by means of the so-called Gauss perturbation equations (Sec. IV). All these results have been obtained for the two Galileos in elliptical orbit, GSAT0201 and GSAT0202.

As regards the determination of the orbits of the satellites, a series of preliminary PODs were performed using the GEODYN II code and applying it to the GSAT0201 (Sec. V) and GSAT0208 (Sec. II of the Supplemental Material [39]) satellites. In this context, a somewhat crude model was deliberately taken for the satellites, that of a cannonball with an area/mass ratio equal to the average one of the Galileo FOC satellites. In the context of the fundamental physics measurements that we are going to make in the near future, a first verification object of our study was to verify if the distribution of the normal points of the laser data is sufficient to obtain the convergence of the state vector. It has therefore been noted that a sufficient number of normal points is not always available to the scientific community, especially for satellites in elliptical orbit. In this regard we have officially requested to the Central Bureau of the ILRS an observation campaign dedicated to the G4S_2.0 project, as was done in the recent past for the GREAT and GASTON (GAlileo Survey of Transient Objects Network) projects. The SLR campaign was approved and began on January 20, 2024. A second verification carried out was to compare the orbits obtained with GEODYN II, again for the GSAT0201 and GSAT0208 satellites, with those we can achieve from the *precise orbits* determined by the IGS analysis centers (Sec. V A and Sec. II of the Supplemental Material [39]). In particular, the orbits obtained by ESOC over the two years of the GREAT project were taken into consideration. The verification was positive, in the sense that even the cannonball model is sufficient to obtain the correct long-term behavior of the orbits of the two satellites considered. We then proceeded to compute the orbital residuals from the orbits obtained in the case of GSAT0201 (Sec. V B). Reliable orbital residuals are an important tool for us to extract from their analysis the signature of the relativistic effects we are interested in, such as the relativistic precessions predicted by general relativity. The residuals we obtained have clearly highlighted the shortcomings of the dynamic model used, in particular the presence of long-term effects with a periodicity of about 365 days, therefore attributable to an inadequate modeling of the direct solar radiation pressure. To test this conclusion, we directly compared the residuals in the orbital elements with the predictions of the box-wing model on the same elements. In fact, the box-wing represents for us a first basic model, we have defined it simplified, toward the construction of more performing models, until hopefully

reaching the FEM of the spacecraft. The comparison was not only positive, but remarkable as almost all of the observed and nonmodeled effects can be replicated with the S-BW model. This result is very significant as it will allow us to enter the accelerations produced by our BW model as input data to the GEODYN II software, as well as those that we will obtain in the future from the spacecraft models that we will gradually develop. This will allow a significant improvement of the dynamic model and therefore the subsequent reduction of tracking data in the POD. This last analysis was introduced in Sec. VI in a preliminary form, where the state of the art of our models was discussed in view of the gravitation measurements that we will have to undertake in the near future.

This work, together with Paper 1 presented in this issue, provides a first overview of the activities and preliminary results of the G4S_2.0 project, which are preparatory to the actual measurements of fundamental physics. Other activities more related to these gravitational measures will be presented in future specific works.

## ACKNOWLEDGMENTS

This work is part of the G4S_2.0 project, developed under the auspices of the Italian Space Agency (ASI) within the frame of the Bando Premiale CI COT 2018 085 under the Accordo Attuativo No. 2021 14 HH.0, with co participation of the Italian Institute for Astrophysics (INAF) and the Politecnico di Torino (POLITO). The authors acknowledge the ILRS (international laser ranging service) Central Bureau for supporting the project objectives through a dedicated SLR campaign and for providing high quality laser ranging data of Galileo satellites. Special thanks to Mike Pearlman (Center for Astrophysics, Cambridge, MA, USA).

[1] D. M. Lucchesi, M. Visco *et al.*, preceding article, Fundamental physics measurements with Galileo FOC satellites and the Galileo for Science project. Part I: a 3D-CAD and a box wing for modeling the effects of nonconservative forces, Phys. Rev. D **109**, 062004 (2024).

[2] https://www.gsc-europa.eu/support-to-developers/galileo-satellite-metadata#6.

[3] G. Bury, R. Zajdel, and K. Sośnica, Accounting for perturbing forces acting on Galileo using a box-wing model, GPS Solut. **23**, 24 (2019).

[4] G. Bury, K. Sośnica, R. Zajdel, and D. Strugarek, Toward the 1-cm Galileo orbits: Challenges in modeling of perturbing forces, J. Geodes. **94**, 16 (2020).

[5] F. Vespe, D. Lucchesi, A. Tartaglia, G. Delle Monache, R. Peron, E. Rosciano, F. Santoli, and M. Visco, GALILEO for Science project (G4S): An opportunity to perform new measurements in fundamental physics, in *Scientific and Fundamental Aspects of GNSS/Galileo. 6th International Colloquium, Valencia (Spain)* (European Space Agency, ESA /ESAC, Spain, 2017).

[6] F. Vespe, GALILEO for Science project (G4S): Eccentric GALILEO satellites for general relativistic investigations, in *42nd COSPAR Scientific Assembly* (COSPAR, Pasadena, CA, 2018), Vol. 42, pp. H0.5-3-18.

[7] D. Lucchesi, G. Delle Monache, R. Peron, E. Rosciano, M. L. Ruggiero, F. Santoli, A. Tartaglia, M. Visco, and F. Vespe, The Galileo for Science (G4S) project: Fundamental physics and space geodesy by the orbit analysis of the Galileo satellites DORESA and MILENA, in *EGU General Assembly Conference Abstracts* (EGU, Vienna, Austria, 2018), p. 15185.

[8] M. L. Ruggiero, A. Tartaglia, D. Lucchesi, G. Delle Monache, R. Peron, E. Rosciano, F. Santoli, F. Vespe, and M. Visco, Fully relativistic positioning for the Galileo for Science (G4S) project, in *EGU General Assembly Conference Abstracts* (EGU, Vienna, Austria, 2018), p. 12644.

[9] https://igs.org/.

[10] H. P. Plag, M. Rothacher, M. Pearlman, R. Neilan, and C. Ma, The global geodetic observing system, Adv. Geosci. **13**, 105 (2009).

[11] S. Herrmann, F. Finke, M. Lülf, O. Kichakova, D. Puetzfeld, D. Knickmann, M. List, B. Rievers, G. Giorgi, C. Günther, H. Dittus, R. Prieto-Cerdeira, F. Dilssner, F. Gonzalez, E. Schönemann, J. Ventura-Traveset, and C. Lämmerzahl, Test of the gravitational redshift with Galileo satellites in an eccentric orbit, Phys. Rev. Lett. **121**, 231102 (2018).

[12] P. Delva, N. Puchades, E. Schönemann, F. Dilssner, C. Courde, S. Bertone, F. Gonzalez, A. Hees, C. Le Poncin-Lafitte, F. Meynadier, R. Prieto-Cerdeira, B. Sohet, J. Ventura-Traveset, and P. Wolf, Gravitational redshift test using eccentric Galileo satellites, Phys. Rev. Lett. **121**, 231101 (2018).

[13] *COMSOL Multiphysics® Reference Manual, Version 5.5*, COMSOL Multiphysics (Burlington, MA, 1998–2019), www.comsol.com.

[14] I. Ciufolini and R. Matzner, Non-Riemannian theories of gravity and lunar and satellite laser ranging, Int. J. Mod. Phys. A **07**, 843 (1992).

[15] D. M. Lucchesi, LAGEOS II perigee shift and Schwarzschild gravitoelectric field, Phys. Lett. A **318**, 234 (2003).

[16] D. M. Lucchesi and R. Peron, Accurate measurement in the field of the Earth of the general-relativistic precession of the LAGEOS II pericenter and new constraints on non-Newtonian gravity, Phys. Rev. Lett. **105**, 231103 (2010).

[17] D. M. Lucchesi, The LAGEOS satellites orbit and Yukawa-like interactions, Adv. Space Res. **47**, 1232 (2011).

[18] R. March, G. Bellettini, R. Tauraso, and S. Dell'Agnello, Constraining spacetime torsion with LAGEOS, Gen. Relativ. Gravit. **43**, 3099 (2011).

[19] D. M. Lucchesi and R. Peron, LAGEOS II pericenter general relativistic precession (1993-2005): Error budget

and constraints in gravitational physics, Phys. Rev. D **89**, 082002 (2014).
[20] B. M. Roberts, G. Blewitt, C. Dailey, M. Murphy, M. Pospelov, A. Rollings, J. Sherman, W. Williams, and A. Derevianko, Search for domain wall dark matter with atomic clocks on board global positioning system satellites, Nat. Commun. **8**, 1195 (2017).
[21] Every satellite has also a Nickname: Doresa and Milena for GSAT0201 and GSAT0202, Oriana and Andriana for GSAT0206 and GSAT0208. Eac nickname corresponds with the name of the child who was the winner of the Galileo Children's Drawing Competition on each European Member State.
[22] See https://www.gsc-europa.eu/system-service-status/orbital-and-technical-parameters.
[23] A. Milani and G. F. Gronchi, *Theory of Orbit Determination* (Cambridge University Press, New York, 2010).
[24] F. Dilssner, T. Springer, G. Gienger, and J. Dow, The GLONASS-M satellite yaw-attitude model, Adv. Space Res. **47**, 160 (2011).
[25] O. Montenbruck, P. Steigenberger, and U. Hugentobler, Enhanced solar radiation pressure modeling for Galileo satellites, J. Geodes. **89**, 283 (2015).
[26] J. Kouba, A simplified yaw-attitude model for eclipsing GPS satellites, GPS Solut. **13**, 1 (2009).
[27] P. Teunissen and O. Montenbruck, *Springer Handbook of Global Navigation Satellite Systems* (Springer, Cham, Switzerland, 2017), 10.1007/978-3-319-42928-1.
[28] Y. Bar-Sever and E. Yoaz, A new model for GPS yaw attitude, J. Geodes. **70**, 714 (1996).
[29] F. Riedel and O. Gülmüs, Observations and operational aspects on the Galileo attitude and orbit control subsystem infra-red radiance variations (2014), p. 3546.
[30] O. Montenbruck, R. Schmid, F. Mercier, P. Steigenberger, C. Noll, R. Fatkulin, S. Kogure, and A. Ganeshan, GNSS satellite geometry and attitude models, Adv. Space Res. **56**, 1015 (2015).
[31] Y. Lou, F. Zheng, S. Gu, and Y. Liu, The impact of non-nominal yaw attitudes of GPS satellites on kinematic $ppp$ solutions and their mitigation strategies, J. Navig. **68**, 718734 (2015).
[32] C. Rodriguez-Solano, U. Hugentobler, P. Steigenberger, and G. Allende-Alba, Improving the orbits of GPS block IIA satellites during eclipse seasons, Adv. Space Res. **52**, 1511 (2013).
[33] E. Schoenemann ((ESA) private communication).
[34] https://www.gsc-europa.eu/support-to-developers/galileo-satellite-metadata##6.
[35] A. Milani, A. M. Nobili, and P. Farinella, *Non-Gravitational Perturbations and Satellite Geodesy* (Adam Hilger, Bristol, 1987).
[36] W. Marquis and C. Krier, Examination of the GPS block IIR solar pressure model, in *Proceedings of the 13th International Technical Meeting of the Satellite Division of The Institute of Navigation* (ION GPS, Salt Lake City, 2000), pp. 407–415.
[37] C. Rodriguez-Solano, U. Hugentobler, and P. Steigenberger, Adjustable box-wing model for solar radiation pressure impacting GPS satellites, Adv. Space Res. **49**, 1113 (2012).
[38] J. I. Andrés de la Fuente, Enhanced modelling of LAGEOS non-gravitational perturbations, Ph.D. thesis, Delft University Press, Sieca Repro, The Netherlands, 2007.
[39] See Supplemental Material at http://link.aps.org/supplemental/10.1103/PhysRevD.109.062005 for results relevant to the satellites GSAT0202 and GSAT0208 concerning, respectively, the application of the simplified box-wing model and precise orbit determination.
[40] O. Montenbruck and E. Gill, *SatelliteOrbits—Models, Methods and Application* (Springer, Berlin, 2005).
[41] https://ilrs.gsfc.nasa.gov/missions/satellite_missions/current_missions/ga01_com.html.
[42] G. Petit and B. Luzum, *IERS Conventions (2010)*, IERS Technical Note 36 (IERS, Frankfurt am Main: Verlag des Bundesamts für Kartographie und Geodäsie, 2010).
[43] A. Einstein, Die Grundlage der allgemeinen Relativitätstheorie, Ann. Phys. **354**, 769 (1916).
[44] J. Lense and H. Thirring, Über den Einfluß der Eigenrotation der Zentralkörper auf die Bewegung der Planeten und Monde nach der Einsteinschen Gravitationstheorie, Phys. Z. **19**, 156 (1918); B. Mashhoon , F. W. Hehl, and D. S. Theiss, On the gravitational effects of rotating masses: The Thirring Lense papers, Gen. Relativ. Gravit. **16**, 711 (1984).
[45] W. de Sitter, On Einstein's theory of gravitation and its astronomical consequences. Second paper, Mon. Not. R. Astron. Soc. **77**, 155 (1916).
[46] D. E. Pavlis *et al.*, *GEODYN II Operations Manual* (NASA GSFC, Greenbelt, 1998).
[47] M. Soffel, S. A. Klioner, G. Petit, P. Wolf, S. M. Kopeikin, P. Bretagnon, V. A. Brumberg, N. Capitaine, T. Damour, T. Fukushima, B. Guinot, T.-Y. Huang, L. Lindegren, C. Ma, K. Nordtvedt, J. C. Ries, P. K. Seidelmann, D. Vokrouhlický, C. M. Will, and C. Xu, The IAU 2000 resolutions for astrometry, celestial mechanics, and metrology in the relativistic framework: Explanatory supplement, Astron. J. **126**, 2687 (2003).
[48] C. Reigber, R. Schmidt, F. Flechtner, R. König, U. Meyer, K.-H. Neumayer, P. Schwintzer, and S. Y. Zhu, An Earth gravity field model complete to degree and order 150 from GRACE: EIGEN-GRACE02S, J. Geodyn. **39**, 1 (2005).
[49] B. D. Tapley, F. Flechtner, S. V. Bettadpur, and M. M. Watkins, The status and future prospect for GRACE after the first decade, in *Eos, Transactions American Geophysical Union Fall Meeting Suppl. Abstract G32A-01* (AGU, San Francisco, CA, 2013).
[50] M. Cheng, B. D. Tapley, and J. C. Ries, Deceleration in the Earth's oblateness, J. Geophys. Res. **118**, 740 (2013).
[51] R. D. Ray, A global ocean tide model from TOPEX/POSEIDON altimetry: GOT99.2, Technical Paper, Report No. NASA/TM-1999-209478, Goddard Space Flight Center, Greenbelt, Maryland, 1999.
[52] E. M. Standish, X. X. Newhall, J. G. Williams, and W. M. Folkner, JPL planetary and lunar ephemerides, DE403/LE403, Technical Report No. JPL IOM 314.10-127, 1995.
[53] C. Huang, J. C. Ries, B. D. Tapley, and M. M. Watkins, Relativistic effects for near-earth satellite orbit determination, Celest. Mech. Dyn. Astron. **48**, 167 (1990).

[54] D. P. Rubincam, P. Knocke, V. R. Taylor, and S. Blackwell, Earth anisotropic reflection and the orbit of LAGEOS, J. Geophys. Res. **92**, 11662 (1987).
[55] D. P. Rubincam, LAGEOS orbit decay due to infrared radiation from earth, J. Geophys. Res. **92**, 1287 (1987).
[56] D. P. Rubincam, Yarkovsky thermal drag on LAGEOS, J. Geophys. Res. **93**, 13805 (1988).
[57] D. P. Rubincam, Drag on the LAGEOS satellite, J. Geophys. Res. **95**, 4881 (1990).
[58] J. O. Cappellari, C. E. Velez, and A. J. Fuchs, Mathematical theory of the Goddard trajectory determination system, NASA STI/Recon Technical Report No. 76N24291, 1976.
[59] A. E. Hedin, MSIS-86 thermospheric model, J. Geophys. Res. **92**, 4649 (1987).
[60] M. Visco and D. M. Lucchesi, Comprehensive model for the spin evolution of the LAGEOS and LARES satellites, Phys. Rev. D **98**, 044034 (2018).
[61] Z. Altamimi, X. Collilieux, and L. Métivier, ITRF2008: An improved solution of the international terrestrial reference frame, J. Geodes. **85**, 457 (2011).
[62] Z. Altamimi, X. Collilieux, and L. Métivier, ITRF2014: A new release of the International Terrestrial Reference Frame modeling nonlinear station motions, J. Geophys. Res. **121**, 6109 (2016).
[63] C. Bizouard , S. Lambert, G. César, O. Becker, and J. Y. Richard, The IERS EOP 14C04 solution for Earth orientation parameters consistent with ITRF 2014 , J. Geodes. **93**, 621 (2019).
[64] P. M. Mathews, T. A. Herring, and B. A. Buffett, Modeling of nutation and precession: New nutation series for nonrigid Earth and insights into the Earth's interior, J. Geophys. Res. **107**, 2068 (2002).
[65] N. Capitaine, P. T. Wallace, and J. Chapront, Expressions for IAU 2000 precession quantities, Astron. Astrophys. **412**, 567 (2003).
[66] This type of orbit modeling is useful when longwavelengths orbit errors, including secular disturbing effects, need to be removed, as well as for long-period resonances and non-gravitational perturbations that are not included in the software dynamical model, as in this case. Experience shows that, while they are useful to improve the fit quality, they can easily bias the estimation of other quantities. See also the discussion in Paper I.
[67] A further observation campaign of three months was carried out by ILRS for the ESA project called GASTON, for the search for dark matter of galactic origin.
[68] https://space-track.org/.
[69] Y. Kozai, The motion of a close earth satellite, Astron. J. **64**, 367 (1959).
[70] T. Springer, NAPEOS mathematical models, and algorithms, Technical Report No. DOPS-SYS-TN-OlOO-OPS-GN, European Space Operations Center (ESA/ESOC), 2009.
[71] K. Nordtvedt, Equivalence principle for massive bodies. II. Theory, Phys. Rev. **169**, 1017 (1968).
[72] C. M. Will, Theoretical frameworks for testing relativistic gravity. II. Parametrized post-Newtonian hydrodynamics, and the Nordtvedt effect, Astrophys. J. **163**, 611 (1971).
[73] C. M. Will and J. K. Nordtvedt, Conservation laws and preferred frames in relativistic gravity. I. Preferred-frame theories and an extended PPN formalism, Astrophys. J. **177**, 757 (1972).
[74] D. M. Lucchesi and G. Balmino, The LAGEOS satellites orbital residuals determination and the Lense-Thirring effect measurement, Planet. Space Sci. **54**, 581 (2006).
[75] C. W. Johnson, C. A. Lundquist, and J. L. Zurasky, The Lageos satellite, International Astronautical Federation Congress, Anaheim, CA, IAF PAPER 76 065 (1976).
[76] D. Lucchesi, M. Visco, R. Peron, M. Bassan, G. Pucacco, C. Pardini, L. Anselmo, and C. Magnafico, A 1% measurement of the gravitomagnetic field of the Earth with laser-tracked satellites, Universe **6**, 139 (2020).